A new seismic stratigraphy in the Indian-Atlantic Ocean gateway resembles major paleo-oceanographic changes of the last 7 Ma

Jens Gruetzner[1], Francisco J. Jimenez Espejo[2], Nambiyathodi Lathika[3], Gabriele Uenzelmann-Neben[1], Ian R. Hall[4], Sidney R. Hemming[5], Leah J. LeVay[6], and the Expedition 361 Scientists[7]

[1]Alfred-Wegener-Institut, Helmholtz-Zentrum für Polar- und Meeresforschung, Am Alten Hafen 26, D- 27568 Bremerhaven, Germany. Jens.Gruetzner@awi.de
[2]Institute of Biogeosciences, Japan Agency for Marine-Earth Science and Technology (JAMSTEC), Natsushima-cho 2-15 Yokosuka 237-0061, Japan*[*]
[3]Ice Core Laboratory, National Centre for Antarctic and Ocean Research (NCAOR), Head Land Sada, Vasco da Gama Goa,403804, India
[4]Department of Earth Sciences, Cardiff University, Main College, Park Place, PO Box 914, Cardiff Wales CF10 3AT, United Kingdom[5]Lamont-Doherty Earth Observatory, Columbia University, 61 Route 9W, Palisades NY 10964, USA
[6]International Ocean Discovery Program, Texas A&M University, College Station TX 77845, USA
[7]See Appendix A2

Key Points:

- New seismic stratigraphy for the late Miocene to Pleistocene at the Agulhas Plateau (IODP Site U1475)
- Reflectors are associated with the onset of the northern hemisphere glaciation, the middle and early Pleistocene transitions, and late Pleistocene glacial/interglacial variability
- Major reorganization of the bottom current circulation pattern at ~ 5.3 Ma due to maximized inflow of North Atlantic Deep Water

[*] now at Instituto Andaluz de Ciencias de la Tierra CSIC - Univ. de Granada, Avda de las Palmeras 4, 18100 Armilla, Spain

Abstract

The exchange of water masses between the Indian Ocean and the Atlantic constitutes an integral inter-ocean link in the global thermohaline circulation. Long-term changes in deep water flow have been studied using seismic reflection profiles but the seismic stratigraphy was poorly constrained and not resolved for the time period from the late Miocene onward. Here, we present results from International Ocean Discovery Program Site U1475 (Agulhas Plateau) located over a sediment drift proximal to the entrance of North Atlantic Deep Water (NADW) into the Southern Ocean and South Indian Ocean. Site U1475 comprises a complete carbonate rich stratigraphic section of the last ~7 Ma that provides an archive of climate-induced variations in ocean circulation. Six marker reflectors occurring in the upper 300 m of the drift are identified here for the first time. The formation of these reflectors is mainly due to density changes that are mostly caused by changes in biogenic vs. terrigenous sediment deposition. Synthetic seismograms allow age assignments for the horizons based on bio- and magnetostratigraphy. Prominent reflectors are related to late Pleistocene glacial/interglacial variability, the middle and early Pleistocene transitions, and the onset of the northern hemisphere glaciation. A peculiar early Pliocene interval (~ 5.3 – 4.0 Ma) bounded by two reflectors is characterized by 4-fold elevated sedimentation rates (> 10 cm/kyr) and the occurrence of sediment waves. We argue that this enhanced sediment transport to the Agulhas Plateau was caused by a reorganization of the bottom current circulation pattern due to maximized inflow of NADW.

1 Introduction

The exchange of shallow and deep water masses between the Indian Ocean and the Atlantic constitutes an integral inter-ocean link in the global thermohaline circulation (THC). The Atlantic Meridional Overturning Circulation (AMOC) in the Atlantic is characterized by a northward cross-equatorial mass flux at the surface ocean, deep water formation in the North Atlantic, and by the southward transport of North Atlantic Deep Water (NADW) in the deeper layers. Below the NADW flow there is an underlying, reversed overturning cell that originates in the Southern Ocean (Ritz et al., 2013).

Modelling studies suggest that buoyancy anomalies in the Atlantic thermocline induced by saline Agulhas waters entrained from the Indian Ocean to the South Atlantic can change the AMOC and hence NADW formation rates (Haarsma et al., 2011; Weijer et al., 2002).

The Agulhas Plateau (AP) in the Southwest Indian Ocean is located in the pathway of the main branch of NADW that takes an eastbound route after passing the southern tip of Africa (Fig. 1). Contourite deposits found on top of the AP, in the Natal valley, and at the Mozambique Ridge (Fischer & Uenzelmann-Neben, 2018; Uenzelmann-Neben, 2002; Wiles et al., 2014) likely bear detailed information on past changes in the NADW flow history over long time intervals of the Cenozoic but until recently only late Pleistocene paleoceanographic studies for the region were carried out using sediment samples obtained from piston cores (Marino et al., 2013; Molyneux et al., 2007; Romero et al., 2015; Ziegler et al., 2013). Long-term changes in deep water flow in the South African gateway during the Cenozoic have been inferred using seismic reflection profiles (Fischer & Uenzelmann-Neben, 2018; Gruetzner & Uenzelmann-Neben, 2016; Tucholke & Carpenter, 1977; Uenzelmann-Neben, 2002; Uenzelmann-Neben et al., 2007). While a recent seismic study of the Mozambique Ridge suggests that bottom current circulation in the African–Southern Ocean gateway may have started as early as the Late Cretaceous (Fischer & Uenzelmann-Neben, 2018), more widespread evidence for a vigorous (proto-Antarctic Bottom Water) circulation has been found for Late Eocene times (Gruetzner & Uenzelmann-Neben, 2016; Tucholke & Embley, 1984; Uenzelmann-Neben et al., 2007). Bottom current sedimentation related to the influence of NADW on the AP may have started within the Middle Miocene to Early Pliocene period (Uenzelmann-Neben et al., 2007).

Previous seismostratigraphic work in the Indian-Atlantic gateway and at the AP (Tucholke & Carpenter, 1977; Tucholke & Embley, 1984; Uenzelmann-Neben, 2001, 2002) is based on ground truth data from piston cores, gravity cores, and dredge samples. Major horizons were related to regional hiati at the Paleocene/ Eocene boundary (reflector LE in Fig. 2), the Early/Middle Oligocene (reflector LO, Fig. 2), the Middle Miocene (reflector MM, Fig. 2), and the Upper Miocene/Lower Pliocene. The Upper Miocene/Lower Pliocene hiatus occurs often very close to the seafloor but can be buried much deeper in sediment drifts identified on the Agulhas Plateau (Uenzelmann-Neben, 2001). Up to now, the seismic stratigraphy on the AP was not constrained by ocean drilling and no further marker horizons have been identified within the time period for the late Miocene to present.

In 2016, the International Ocean Discovery Program (IODP) Expedition 361 drilled six sites on the southeast African margin and in the Indian-Atlantic ocean gateway, southwest Indian Ocean. The sites were targeted to reconstruct the history of the greater Agulhas Current system and to determine the dynamics of the Indian-Atlantic gateway circulation over the past ~5 Ma. At all sites, the recovered sequences allowed the generation of complete spliced stratigraphic sections for the upper 200 to 300 m (Hall et al., 2017b), which will help to refine the Plio-Pleistocene seismic stratigraphy for the area.

In this paper, we present a new detailed seismostratigraphic model for the uppermost 300 m (~ 7 Ma to present) of the AP which is based on a detailed correlation of edited, spliced, and in situ corrected density and velocity data from Site U1475 (IODP Exp. 361) with site survey seismic reflection profiles. The results from seismic modeling via synthetic seismograms are interpreted in combination with measurements of natural gamma radiation (NGR) and carbonate content to infer major changes in sediment composition that are related to variations in bottom current controlled sedimentation in the Indian-Atlantic Ocean gateway.

2 Geologic and oceanographic setting of the Agulhas Plateau

The AP is a major bathymetric high in the Southwest Indian Ocean (Fig. 1a). It was formed during the early stages of the opening of the South Atlantic as part of a greater Southeast African Large Igneous Province (LIP) in phases of highly varying magmatic and volcanic activities between ~140 and 95 Ma (Gohl et al., 2012). The main volcanic formation of the greater AP can be estimated to have taken place between ~100 - 94 Ma (Parsiegla et al., 2008) when the region passed over the Bouvet hotspot. Today, the AP ascends to ~2500 m above the adjacent seafloor, and the 230,000 km^2 area has a sedimentary cover of variable thickness. While the northern part of the plateau is characterized by rugged topography with relatively thin and irregularly distributed sediments, the central and southern parts exhibit a smoother topography with a more uniform and thicker sediment cover (Allen & Tucholke, 1981; Uenzelmann-Neben, 2001). The AP is flanked by deep basins, the Agulhas Passage in the North, the Agulhas Basin in the West, and the Transkei Basin in the Northeast (Fig. 1a).

The AP region is characterized by a strong water mass transport at all depth levels (Hernández-Guerra & Talley, 2016; Macdonald, 1993). The surface circulation is dominated by the Agulhas Return Current (Lutjeharms & Ansorge, 2001), which flows eastward over the AP and can reach down to more than 1500 m (Lutjeharms, 2007). The Agulhas Return Current originates from the Agulhas Retroflection south of Cape Agulhas where the Agulhas Current (AC) takes an anti-clockwise turn and doubles back on itself (Fig. 1a). The remainder of the warm and saline surface and intermediate waters from the Indian Ocean leaks into the

Atlantic (Beal et al., 2011) via Agulhas Rings (Arhan et al., 2011) transporting between 5-20 Sv of water from the Indian Ocean to the South Atlantic. Below the AC (~ 1000 – 2000 m) Antarctic Intermediate Water (AAIW) originating from surface water around Antarctica also follows the same flow path near South Africa as the Agulhas Current and shows a similar retroflection (Lutjeharms, 1996). The top of the AP is located within the core flow of present-day North Atlantic Deep Water (NADW), which exits the South Atlantic to the Indian Ocean around the tip of South Africa within a broad slope current. NADW can be identified by its higher salinity (S = ~34.8 psu, Figs. 1b,c) (Boyer et al., 2013) and more negative radiogenic Neodymium (εNd = ~-10 to -10.5) signature (Stichel et al., 2012) compared to Southern Ocean derived Upper (UCDW)- and Lower Circumpolar Deep Water (LCDW) masses (S = 34.6–34.7 psu, , Fig. 1b,c) (Arhan et al., 2003). At depths below 4000 m the flanks of the AP are bathed by different branches of LCDW taking northeast directed pathways into the Indian Ocean.

2.1 IODP Site U1475

IODP site U1475 is located in 2669 m water depth on the southwestern flank of the AP over a wedge-shaped sediment drift, which thickens to the west reaching a water depth of ~2510 m at its crest (Figs. 1, 2). Further towards the west, internal reflectors of the drift are truncated at the seafloor indicating erosion while no indications for major current erosion have been found on the eastern side of this drift (Uenzelmann-Neben, 2001). The recovered cores comprise a complete stratigraphic section for the upper 280 m based on a splice constructed from five parallel holes (Hall et al., 2017c).

The sediment recovered at Site U1475 was classified in two lithologic units. The very thin Unit I (0–4.75 m CSF-A, Fig. 3e) is composed of pale brown, light greenish or olive-gray, and white-gray nannofossil-rich foraminifer ooze. Unit II (4.75–277.22 m CSF-A, Fig. 3e) is composed of light greenish or pale gray to white-gray nannofossil ooze. Alternations between foraminifer-bearing or foraminifer-rich nannofossil ooze and nannofossil ooze with fine sand (foraminifers, quartz, and occasionally diatoms) were observed. In general the recovered sediment is quite uniform without primary sedimentary structures and predominantly consists of biogenic materials. Centimeter-scale diffused mottling is common and indicates widespread bioturbation. While in Lithologic Unit I sand sized foraminifera constitute the main sediment component (45 ± 5% on average), the biogenic fraction of the remaining section (Lithologic Unit II) is fine grained (67 ± 10% clay size), dominated by calcareous nannofossils (55 ± 11% on average), and classified as nannofossil ooze (Hall et al., 2017c). The non-carbonate fraction consists mainly of quartz (11 ± 4% on average), clay minerals (3 ± 2%) and diatoms (6 ± 4%). The presence of pyrite is also common while glauconite and feldspar occur rarely. Shipboard measurements revealed that calcium carbonate content in weight percentage ($CaCO_3$ wt%) is ~80 wt% on average and ranges between 74 wt% and 86 wt%. Shipboard bio- and magnetostratigraphic data (Hall et al., 2017c) indicate that the sedimentary sequence extends back to the late Miocene (~7 Ma). Between the bottom of Site U1475 at ~7.5 Ma and 5.3 Ma, average sedimentation rates are ~2.5 cm/ky. After ~5.3 Ma the sedimentation rates increase significantly and these elevated rates (10.3 cm/ky) last until to ~3.9 Ma. At ~3.9 Ma sedimentation rates drop again to an average rate of 2.9 cm/ky.

3 Methods

For this study, the raw IODP Site U1475 shipboard physical property data of *P-wave* velocity (V), bulk density (WBD), and natural gamma radiation (NGR) measured during IODP Exp. 361 (Hall et al., 2017c) have been edited and cleaned of outliers (Fig. 3). While V and WBD data have been further converted to in situ conditions and were used to calculate synthetic seismograms, wt% Potassium (K) derived from the NGR spectra is used as an indicator of terrigenous vs. biogenic sediment composition.

Concerning the usage of depth scales we follow the newest conventions of IODP (IODP-MI, 2011). Raw data were recorded on the CSF-A depth scale equivalent to the formerly used meters below seafloor (mbsf) scale. Composite curated depth below sea floor (CCSF) scales are used for the presentation of spliced data from multiple holes. Due to the methodology of splicing the CCSF depth scales are extended relative to CSF-A (Lisiecki & Herbert, 2007). At Site U1475 the extension is on average 9.5% for all holes. Thus to correct for the depth offset a 9.5% linear compression was applied to the entire depth so that the compressed core length (CCSF-B) was equal to the interval cored. An extensive description of the depth scales is given in the supporting information.

3.1 Measurements

P-wave velocity (V) was measured at a resolution of 2.5 cm at all holes drilled at Site U1475 using a *P-wav*e logger mounted on the whole round multi sensor track (Hall et al., 2017a). The logger transmits an ultrasonic (500 kHz) *P-wa*ve pulse across the core section (Schultheiss & McPhail, 1989), and the traveltime of the signal is determined by a processing software that automatically detects the first arrival of the *P-wa*ve to a precision of 50 ns.

Wet bulk density data was obtained at 2.5 cm resolution on the whole round multi sensor track (Hall et al., 2017c) using a Gamma Ray Attenuation (GRA) densitometer with a principal energy peak at 0.662 MeV (Best & Gunn, 1999). GRA-bulk density is calculated from the measured attenuation of a gamma beam transmitted through the core (Davidson et al., 1963). The attenuation through Compton scattering is related to the electron density in the sediment and can be used to derive bulk density by assuming an average attenuation coefficient of the sediment (Evans, 1965; Gerland & Villinger, 1995). Additionally, wet bulk density (WBD) was directly determined on 90 discrete samples by measurements of weights and volumes (wet and dry). These measurements also allow us to calculate dry bulk density, grain density, void ratio, and porosity (Hall et al., 2017a). Changes in GRA-bulk densities and WBD are well correlated throughout Site U1475 with slightly lower absolute values for the GRA densities (Fig. 4a). We thus converted the GRA-bulk densities to wet bulk densities using the relationship WBD = 1.008*GRA-density - 0.0508. This highly linear equation (r^2 = 0.93) is derived from regression analysis of WBD measurements at Site U1475 and corresponding GRA-density measurements across the same depth interval (Fig. 4b). Subsequently, we used the linear relationships (Figs. 4c,d) between WBD vs. dry bulk density (r^2 = 0.99) and WBD vs. porosity (r^2 = 0.95) to derive high-resolution (2.5 cm) data sets of dry bulk density and porosity, respectively. While the corrected dry bulk densities are provided for upcoming environmental studies based on the calculation of millennial-scale resolution sediment accumulation rates, porosity is used for the in situ correction of P-wave velocities (see 3.3).

A Natural Gamma Radiation Logger equipped with 8 Sodium Iodide (NaI) scintillator detectors, 7 shielding plastic scintillator detectors, 22 photomultipliers, and passive Lead shielding (Vasiliev et al., 2011) was used to measure gamma radiation emitted from the whole-round core sections of Site U1475 at a resolution of 10 cm (Hall et al., 2017c). Changes in natural gamma radiation (NGR) represent the total variation in activity of the radioactive elements ^{40}K (Potassium), ^{238}U (Uranium), and ^{232}Th (Thorium), and by integration of the NGR counts over the element-specific energy intervals of the spectrum concentrations of U, Th, and K have been derived (De Vleeschouwer et al., 2017). K is common in many sediments which bear feldspar, mica, and clays, thus characterizing the terrigenous sediment fraction.

Following core splitting, spectral color reflectance was measured at resolutions of 0.5 or 1 cm on the archive-half sections using an Ocean Optics USB4000 spectrophotometer with a halogen light source and an additional blue light source (Hall et al., 2017a). The measurements cover a wavelength range through the visible spectrum and slightly into the infrared domain (400 - 900 nm). Each measurement was recorded in 2 nm wide spectral bands and also converted to the L*a*b* system, which is also referred to as the CIELAB system. In this study we use color reflectance (Lightness parameter L*) to validate the shipboard age model for the Pleistocene by comparing it the global benthic oxygen isotope stack (see 5.3).

3.2 Physical property editing

During high recovery expeditions like Exp. 361, a vast number of physical property measurements are taken by core scanners in relatively short time to maintain a constant core flow. Immediately after each scanner run, the measurements are saved to the IODP data base (http://web.iodp.tamu.edu/LORE/) to provide data sets that can be used rapidly for stratigraphic correlation between multiple holes during the cruise. These time constraints do not allow for much quality control by the operators, and subsequently the saved records usually contain a number of outliers (Fig. 3), which are mostly caused by section breaks and core disturbance. Although sediment disturbance through drilling at Site U1475 was minimized using the advanced piston corer, bad weather conditions caused significant heave and often led to core disturbance. When constructing the splice, these “bad intervals” were usually avoided, and thus the number of outliers are reduced in the composite section. Nevertheless, some outliers remain in the “splice”. The highest number of “spikes” is commonly found in the *P-wave* velocity measurements (Fig. 3b) since these are most delicate because a very good acoustic coupling between transducers, core-liner, and sediment is required to allow propagation of the compressional-wave pulse with sufficient amplitude. Otherwise the signal is strongly attenuated, the automated picking of the first arrival becomes inaccurate and anomalously high or low velocities are calculated. Velocities below 1400 m/s and above 4000 m/s were automatically omitted during the scanning process. The remaining questionable velocity values were judged manually by comparing the data with the digital core images, core descriptions, and stored waveform data. Sometimes step-like changes in the velocity values of more than 50 m/s were observed. This mostly occurred because the automated detection algorithm missed one or more minima, and in these cases the velocity was recalculated using manually adjusted traveltime picks. Anomalous data that corresponded to either a section end or visual core disturbance were deleted. Due to this rigorous editing process data gaps larger than 10 cm appeared at several places in the velocity splice. These were filled by data from parallel holes not used for the splice. The procedure to map the off-splice holes into the CCSF-D scale is described in the supplementary information. The longest interval covered by off-splice data occurs in the upper 3.95 m below the seafloor where the anomalously low velocities (< 1400 m/s) recorded for the primary splice (Hole U1475B) were replaced with data from Hole U1475C. In total, only 8% of the used velocity data are from off-splice holes.

3.3 In situ correction

For an accurate correlation of seismic stratigraphies with geologic events identified in boreholes it is necessary to adjust the acoustic impedance derived in the laboratory to the natural conditions in the sub-seafloor environment (in situ correction, Fig 3). Differences between laboratory and in-situ measurements can be caused by temperature changes, pressure reduction, decrease of sediment rigidity, and mechanical porosity rebound (Hamilton, 1976) from which the effect of overburden pressure reduction on sediment elastic moduli and thus *P-wave* velocity is the most significant factor in carbonate rich sediments (Urmos et al., 1993). An in situ velocity correction for carbonate sediments was empirically derived from wells on the Ontong Java Plateau (Urmos & Wilkens, 1993; Urmos et al., 1993) and was successfully tested for oozes and chalks recovered at ODP Sites 704, 722, and 762. This correction applied here for the Site U1475 velocity data consists of two steps.

A first correction accounts for in situ temperature and pressure of the pore fluids (Wyllie et al., 1956):

$$\frac{1}{V_{corr}} = \frac{1}{V_{lab}} + \left[\left(\frac{\eta}{V_{w\ in\ situ}}\right) - \left(\frac{\eta}{V_{w\ lab}}\right)\right]$$

with η = fractional porosity, V_{corr} = temperature and pressure corrected velocity, V_{lab} = measured laboratory velocity, $V_{w\ in\ situ}$ = velocity of sea water at in situ temperature, depth (pressure) and salinity (35 %) (Mackenzie, 1981), and $V_{w\ lab}$ = velocity of sea water at laboratory conditions (Mackenzie, 1981).

A second adjustment corrects the differences in elastic moduli and sediment rigidity

$$V_{in\ situ} = V_{corr} + 0.66 \times (1 - e^{-0.00208 \times d})$$

with $V_{in\ situ}$ = velocity under in situ conditions, V_{corr} = temperature and pressure corrected velocity, and d = depth (in m).

The effects of hydraulic rebound on bulk density and porosity at Site U1475 have been calculated by considering the difference between laboratory and in situ sea water densities (Millero et al., 1980) but the rebound effect is smaller (< 1 %) than the measurement uncertainties and is thus neglected for the purpose of this investigation.

3.4 Synthetic seismograms

Synthetic seismograms calculated to correlate the borehole information (on depth) with the seismic reflection pattern (on traveltime) are based on an accurate depth to time conversion via the obtained velocity information. The in-situ corrected P-wave velocity and density data were used to calculate acoustic impedance ($I = V_{in\ situ} \cdot WBD$) and reflection coefficients ($R = (I_2 - I_1/I_2 + I_1)$). The synthetic seismograms are a convolution of the reflection coefficients with an artificial wavelet (Ricker, 1953). Ricker-wavelets in the frequency range between 20 and 150 Hz were tested. The applied wavelets of lower frequencies bear a loss of resolution while high-frequency wavelets introduce reflectors, which are not observed in the seismic data. The convolution of the reflectivity series with a 65 Hz Ricker wavelet correlated best with the seismic data and therefore was used to generate the synthetic seismograms. No filters were applied to the synthetic seismograms.

3.5 Age model

Age control of the interpreted seismic reflectors is based on the shipboard age model for Site U1475 (Fig. 3a) that was derived from time estimates based on a combination of major planktonic foraminifer, calcareous nanno-plankton, diatom, and paleomagnetic datums. Fits of linear models to the available data with correlations of $r^2 = 0.94$ (0–3.9 Ma), 0.92 (3.9–5.3 Ma), and 0.68 (5.3–7.5 Ma) suggest that linear sedimentation rates represent a good approximation of deposition rates for at least the Pliocene and Pleistocene parts of the record (Hall et al., 2017c). Examination of the Pliocene–Pleistocene sequence of chronological events since 3.9 Ma shows modest but consistent mismatches between datums at the same depth levels (Hall et al., 2017c) which give an indication of the maximum uncertainties inherent to the model and allow to estimate errors associated with stratigraphic placement of the seismic reflectors. The estimated errors are ±0.50 Ma at 260 m CCSF-A, ± 0.40 Ma at 100 m CCSF-A, ± 0.30 Ma at 50 m CCSF-A (Fig. 2a). For the upper 30 m CCSF-A (~ last 1 Ma) the parameter L* (Lightness) exhibits amplitude changes nicely reflecting glacial/interglacial cycles and the L* curve (see 5.3) plotted on the linear shipboard age model reveals a great similarity with a global benthic isotope stack (Fig. 10b). A peak to peak correlation of identified marine isotope stages (MIS) shows that errors in the age determination of reflectors within the last 1000 kyrs are less than ± 0.03 Ma.

4 Results

The raw laboratory shipboard physical property records of *P-wave* velocity and density are described in the IODP Exp. 361 report for Site U1475 (Hall et al., 2017c). We here report major changes in acoustic impedance (in units of 10^5 g · s^{-1} · cm^{-2}) derived from in situ corrected velocity and density data that occur on the CCSF-B (mbsf) depth scale (Fig. 5). Acoustic impedance at Site U1475 (Fig. 5c) is 2.65 on average and varies between 1.97 and 3.12 (Fig. 6). It increases from 2.33 at the seafloor to 2.87 at 277 m CCSF-B exhibiting a linear increasing trend (r^2 = 0.88) with depth (1.73 m^{-1}) that is due to porosity reduction by compaction with increasing overburden pressure. Residual fluctuations around this trend are likely due to variation in sediment composition. Spike like impedance minima occur within the upper 10 m and between 20 m and 25 m CCSF-B. Below, two very prominent steps to higher impedance at 117 m and to lower impedance at 242 m are observed. Between these steps several cm scale high impedance spikes occur at 142 m, 172 m, 214 m, 220 m, and 228 m CCSF-B. A comparison of the curves displayed in Figure 5 reveals that impedance shows a greater similarity with density than with velocity. To further examine the variation in impedance, linear regressions between these parameters were calculated. There is a very good correlation (r^2 = 0.85) between velocity and impedance (Fig. 6a) but the density-impedance correlation (Fig. 6b) is even stronger (r^2 = 0.97). The low-resolution shipboard wt% $CaCO_3$ data (Hall et al., 2017c) also allow a test of the carbonate vs. physical property relationships at Site U1475 (Fig. 7). Acoustic impedance (Fig. 7a) and density (Fig. 7b) both exhibit a strong positive correlation (r^2 = 0.50) with carbonate content.

Potassium (K) content derived from NGR (De Vleeschouwer et al., 2017) ranges from 0.11 wt% to 0.86 wt% with an average of 0.46 wt% (Fig. 5d). In the upper 30 m CCSF-B, K values show the most pronounced variations, with high amplitude cyclic changes around 0.45 wt%. Following an increase at 30 m CCSF-B, K values fluctuate with longer wavelength and lower amplitude around an average 0.6 wt% down to 100 m CCSF-B. From 100 to 230 m CCSF-B K-content decreases from 0.6 to 0.3 wt% and shows very harmonic fluctuations that can be related to cyclic changes in the amount of carbonates vs. terrigenous components. At 230 m CCSF-B, wt% K exhibits a strong increase to 0.5 wt% and at 242 m CCSF-B, another wt% K maximum correlates with the step-like decrease in impedance. NGR at Site U1475 is inversely correlated to wt% $CaCO_3$ (Fig. 7c), which indicates the dilution of biogenic carbonate with terrigenous derived particles. Potassium content (wt% K) derived from NGR shows an even stronger anti-correlation with $CaCO_3$ (Fig. 7d). Thus in the discussion we use the wt% K curve to characterize the climate related development of the seismic reflectors.

Six seismic reflectors (Table 1) of high to moderate amplitude occurring within the upper 300 m of the sediment column at the AP and described here for the first time are unambiguously correlated with the synthetic record (Figs. 8,9). In the seismic profile AWI-98014 (Fig. 9) high amplitude reflections are observed below ~4 s TWT (not drilled) and in the upper 60 ms TWT below the seafloor (reflectors Purple and Green). The remaining section reveals very low to moderate seismic amplitudes. While the sediments between reflectors Green, Orange, and Yellow appear rather transparent in the seismic section, buried undulating wavy sedimentary structures are visible between reflectors Red and Yellow. The wavy reflection pattern occurs in a transparent interval in Fig. 2 and is relatively faint in Fig. 9 (a,b). But a black and white plot using a narrow bandpass filter (Hanning window, 40–45

Hz and 210–230 Hz) shows the development of sediment waves above reflector Red (after ~ 5.6 ± 0.5 Ma) more clearly (Fig. 9c). The wavelength of these structures is ~5 km and their height degrades from ~ 29 m at reflector Red towards the seafloor.

5 Discussion

5.1 Physical property interrelationships and the origin of seismic reflectors

The observed very high density-impedance correlation in comparison to a weaker velocity-correlation at Site U1475 (Fig. 6) has been reported also for other areas with a high percentage of carbonate sedimentation (Mayer et al., 1985), and can be explained by the relatively minor degree of fluctuation in sonic velocity (< 5% of its mean value) compared to the much higher degree of variation in bulk density (~ 23% of its mean value). This implies that density can be used as a predictor for acoustic impedance in the Agulhas area and that vice versa understanding impedance contrast and thus the formation of seismic reflectors is mainly a task of determining what causes changes in saturated bulk density, or its inverse, porosity.

For carbonate sediments of the equatorial Pacific it was found that density and impedance changes are strongly controlled by variations in carbonate content (Mayer, 1980; Mayer et al., 1986; Reghellin et al., 2013). High-carbonate samples are dominated by high-density platy carbonate material while low-carbonate material is dominated by low-density spiny siliceous microfossils. Thus when the percentage of carbonate is high, the percentage of biogenic silica is low and this composition results in increased saturated bulk density and thus increased impedance. At Site U1475 the %CaCO3-impedance correlation is positive and strong (Fig. 7) but not as perfect as for the equatorial Pacific (Mayer, 1991). This is most likely due to the generally quite low variability of $CaCO_3$ at the AP (74 – 85%). Further in contrast to the equatorial Pacific, the non-carbonate fraction at U1475 is dominated by quartz (11% ± 4% on average) and not by siliceous microfossils. Diatoms are continuously present in the sediment at Site U1475 but with much lower percentages (5% ± 2%) compared to the equatorial Pacific.

5.2 Major depositional changes during the late Miocene and Pliocene

Since Site U1475 today is bathed by NADW, we here discuss significant changes in oceanographic parameters (mainly changes in NADW inflow) that took place at or close to the same time the seismic reflectors were generated to assess their paleoceanographic significance for the Indian-Atlantic gateway. The changes in the physical property records are described in an upward direction in order to discuss the paleo-oceanographic events chronologically.

The deepest major seismic horizon tied to the U1475 boreholes, reflector Red (Fig. 9), is associated with a very strong upward impedance increase (Fig. 8) resulting from step like changes in density and velocity at 242.39 m CCSF-B (Fig. 5). At this depth, an upward decrease in wt% K is observed (Fig. 5d) but this change of 0.1 wt% K is small when compared to other intervals, especially the uppermost 50 m CCSF-B where short term changes of up to 0.3 wt% K occur. This suggests that changes in the admixture of terrigenous derived sediments to the biogenic carbonate fraction are likely not the cause for the high impedance contrast at 242.39 m CCSF-B. High *P-wave* velocities can be caused by elevated sand content, and thus grain size changes may be the cause for the impedance contrast. Given the discussed dating uncertainty of ± 0.5 Ma, reflector Red occurs within the late Miocene (5.2 - 6.2 Ma) in an interval with significant variability in benthic $\delta^{18}O$, including the prominent glacial marine isotope stage (MIS) TG20 (Hodell et al., 2001). Widespread erosion documented around Antarctica indicates a vigorous ACC during this time. Furthermore, a drastic sea level fall during this period of maximum Antarctic ice volume at ~ 6 Ma is considered to have triggered the Messinian salinity crisis, during which the

Mediterranean Sea was periodically blocked from and connected again with the North Atlantic (Ohneiser et al., 2015). Related changes from more to less saline Mediterranean Outflow Water could have caused significant reductions in AMOC (Ivanovic et al., 2014) and thus in NADW transport to the Southern Hemisphere.

Reflector Red has a wavy outline, and this wavy character of the subsurface seismic reflection pattern continuous upward towards reflector Yellow (Fig. 9c) indicating the development of sediment waves after ~ 5.6 ± 0.5 Ma. Such deep-sea sediment waves are symmetrical undulating bedforms developing under stable bottom flow conditions (Wynn & Masson, 2008). They can occur under turbidity current and geostrophic flow systems (McCave, 2017; Wynn & Stow, 2002). Downslope sediment flows and river-fed turbidite systems have been described for the eastern margin of southern Africa (Castelino et al., 2017; Wiles et al., 2013) but the Site U1475 sediment cores from the elevated top of the AP do not show any turbiditic sedimentary structures (Hall et al., 2017c). Thus we interpret the sediment waves on the AP, which developed contemporaneously to a wavefield at the same latitude in the western Atlantic (Gruetzner et al., 2014), to be shaped by contouritic bottom currents. A model of sediment wave formation (Flood, 1988) predicts that the observed wave dimensions at the AP can form under geostrophic flow velocities that range from ~8 to 17 cm/s and the observation that the wave crests do not exhibit a significant up-current migration would point towards flow velocities at the lower end of this range. Present day bottom water flow speeds for the southwestern AP are in the range of ~2 to 6 cm/s as derived from high-resolution global ocean circulation models (Cronin et al., 2013).

At the AP the sediment wave development is accompanied by a dramatic increase in sedimentation rates from 2.8 to 10.3 cm/kyr at ~ 5.3 Ma (Fig. 3a). Together, the elevated sediment accumulation and the appearance of sediment waves suggest a significant change in bottom current derived sediment transport to the AP after ~ 5.6 ± 0.5 Ma.

Other processes such as increased productivity or higher terrigenous supply could have also caused the increased sedimentation rates but wt% K does not indicate a significant change in the biogenic vs. terrigenous sediment composition and also the $CaCO_3$ percentages do not change (Fig. 5d). In case of a massive increase in biogenic carbonate production over the AP, one would expect an increase in carbonate content and lower K percentages. Conversely, higher terrigenous supply would result in lower carbonate content and increased K percentages. Biosiliceous sedimentation at site U1475 is slightly higher between 185 and 245 m CCSF-A (~ 4.6 – 5.2 Ma) (Hall et al., 2017c) but can also not account for the almost 4-fold increase in sedimentation rates. The profound change in sedimentation rate at the AP occurs in a time interval for which an increase of NADW production (Poore et al., 2006), a strengthening of AMOC (Karas et al., 2017), and a sustained interval of high (3 times the present day value) %NCW in the southern ocean (Billups, 2002) have been inferred. We conclude that these profound changes in global ocean circulation, that are thought to be related to the closure of the CAS below a critical level (Karas et al., 2017), likely increased the intensity and lowered the core flow of the south setting bottom water current over the southwestern AP (Fig. 1b) in such a way that drift growth at the AP could accelerate. These changes in the Indian-Atlantic Ocean gateway occurred contemporaneously with other regional oceanographic and climatic variations, such as an abrupt change from dry to humid climate conditions in northwest Australia (Christensen et al., 2017) and an expansion of the Western Pacific Warm Pool (WPWP) to the South China Sea (Brierley et al., 2009) and eastern Indian Ocean (Karas et al., 2011).

Reflector Yellow (Figs. 8, 9) marks the upper boundary of the high sedimentation rate interval at 117 m CCSF-B (Table 1) and is caused by step-like upward drops in acoustic impedance, density, and velocity (Fig. 5). The reflector occurs in an interval (~ 4 ± 0.4 Ma) characterized by a number of high wt% K (low wt% $CaCO_3$) peaks (Fig. 10d) indicating enhanced deposition of terrigenous derived sediments. In the global benthic isotope stack, this time is marked by "cold" stages MIS Gi22/Gi20 (Fig. 10) corresponding to a pronounced early Pliocene expansion of global ice volume (Lisiecki & Raymo, 2005) and to a drop (-50 m) in the eustatic sea level curve (Miller et al., 2005). Thus reflector Yellow likely marks a transition to colder conditions and the associated wt% K peaks may reflect a higher input of atmospheric dust into the depositing bottom currents e.g. through more vigorous atmospheric circulation and/or extended dust source areas due to reduced vegetation cover.

Across reflector Yellow, a drop in sedimentation rates from 10.3 cm/kyr back to 2.8 cm/kyr (Fig. 3) and the disappearance of the wavy structure of the subsurface reflections (Fig. 9) indicate another major modification in depositional conditions. This shift might be due to a weakening of the AMOC between ~3.8 and 3 Ma that is inferred from interhemispheric temperature and $\delta^{18}O_{seawater}$ gradients (Karas et al., 2017) as well as from benthic $\delta^{13}C$ records from the Southeast Atlantic (Bell et al., 2014; Billups, 2002). The weakening is considered as a complex climatic effect of global cooling possibly supported by tectonic changes in the Indonesian region (Karas et al., 2017). Sediments between reflectors Yellow and Orange form a relative transparent sheet-like seismic unit (Fig. 9) suggesting that depositional conditions prevailing from ~ 4 to 2.7 Ma were tranquil and stable (Stow et al., 2008).

Reflector Orange at 71 m CCSF-B (Fig. 5, Table 1) has moderate strength and correlates with a step-like upward decrease in impedance (Fig. 10c) and a local maximum in wt% K (terrigenous supply). The assigned age of ~2.7±0.3 Ma places the reflector in an interval with distinct steps of abrupt change in the stacked benthic $\delta^{18}O$ record (Lisiecki & Raymo, 2005) occurring ~3.0–2.7 Ma (Fig. 10a, c). Considering the age uncertainty the wt% K spike at Site U1475 and reflector Orange are likely related to one of the larger $\delta^{18}O$-maxima (cold stages) MIS G10 or MIS G6. These steps are thought to mark the onset of Quaternary-style climates (Lisiecki & Raymo, 2005) associated with the intensification of

Major Northern Hemisphere glaciation (iNHG). However, a novel sea-level reconstruction (Rohling et al., 2014) implies that the changes in benthic $\delta^{18}O$ at ~2.7 Ma were mainly driven by deep sea cooling and that the first major glaciation (sea level below 270 m) occurred much later at ~2.15 Ma (MIS 82). A crucial role as potential forcing for the onset of Quaternary-style climates is attributed to the final closure phase of the Central American Seaway (CAS) dated to 3.2–2.7 Ma on the basis of the growing gradient in sea surface salinity between the southwest Caribbean and eastern equatorial Pacific (Sarnthein, 2013; Steph et al., 2006). Our new seismic stratigraphy reveals that depositional changes at the AP leading to the formation of reflector Orange at ~2.7±0.3 Ma occurred contemporaneously to the final closure of the CAS rather than to the sea level lowering at MIS 82 (2.15 Ma, Fig. 10c). However, relatively constant sedimentation rates and the rather low seismic amplitudes above reflector Orange (Fig. 8) do not indicate massive changes in bottom water flow over the AP following the iNHG.

5.3 Reflectors related to Pleistocene climate variability

Reflector Blue (Fig. 8, Table 1) is caused by sharply upward increasing impedance above a minimum in density at 40 m CCSF-B (Figs. 5, 10c). At this depth, wt% K decreases from a local maximum of moderate amplitude. This change in wt% K and the assigned age of ~1.5±0.3 Ma suggests that reflector Blue may be related to enhanced carbonate sedimentation at the transition from glacial conditions towards the “warmer” interglacials MIS 47/49 (Fig. 10a). Interestingly, the absolute maximum (Fig. 5d) in wt% K at 45 m CCSF-B (~1.7 Ma) is not reflected in an impedance/density reduction and thus does not cause a seismic reflector. Benthic carbon isotope records and gradients indicate that, corresponding to a decrease in the ventilation of the CDW (Hodell & Venz-Curtis, 2006), glacial shoaling of NADW began or increased greatly at ~1.5 Ma (Lisiecki, 2014). As a consequence of the NADW shoaling sedimentation on the AP may have been increasingly influenced by glacial/interglacial changes in the depth of the NADW/CDW boundary since 1.5 Ma.

Two high amplitude seismic reflectors (Purple and Green) are visible directly below the seafloor reflection (Figs. 8, 9) and occur within the upper 25 m CCSF-B (Table 1). In this interval WT% K shows large scale oscillations in amplitude corresponding to late Pleistocene glacial/interglacial cycles. Both reflectors result from large impedance contrasts occurring in intervals characterized by upward increasing WT% K values (Fig. 10b) suggesting that the reflectors were caused by enhanced terrigenous derived supply (carbonate minima). From piston core studies covering the last 350 kyrs it is known that glacial intervals (even MIS) at the AP are characterized by lower carbonate percentages, higher biogenic opal content (Romero et al., 2015), and the occurrence of macroscopically visible dropstones, probably corresponding to ice rafted debris (IRD) (Marino et al., 2013). Thus the WT% K maxima corresponding to reflectors Purple and Green likely indicate glacial conditions. The bio- and magnetostratigraphic age control places the WT% K maxima at glacial marine isotope stages MIS 10 and 20.

Based on the linear age model (Fig. 3a) reflector Green can be dated at ~0.8 Ma corresponding to glacial MIS 20. But the L* to LR04 correlation (Fig. 10b) before 0.65 Ma is not unambiguous, and thus the reflector may also relate to stage MIS 22 (0.87 Ma) implying an uncertainty of <100 kyr in the shipboard age model. MISs 20 and 22 are both within the mid-Pleistocene transition (MPT), the time period when glacial-interglacial periodicity increased from ~41-thousand-year to 100-thousand-year cycles and developed higher-amplitude climate variability (Hays et al., 1976). Nd isotope data from the Cape Basin indicate a major THC-weakening (THC-crisis) during the MPT between MISs 25 and 21 (~0.95 to 0.86 Ma ago) and subsequently weaker export of NADW during the following glacials (Pena & Goldstein, 2014). Thus the impedance contrast originating from rapid changes in terrigenous supply that formed reflector Green can be interpreted to reflect rapidly changing sediment transport to the AP by variable NADW during the THC-crisis. Upward from reflector Green the so-called interval of “luke warm interglacials” (MIS 19-13) (Jaccard et al., 2013) is characterized by very low variability in acoustic impedance (Fig. 10b), which at Site U1475 commences into MIS 11.

Although the uncertainty of the used bio- and magnetostratigraphic datums is estimated to be up to ±0.3 Ma for the late Pleistocene (Fig. 3a), we are confident that the association of reflector Purple with the MIS 10/11 transition on the linear age model for the last 1 Ma is accurate since the associated wt% K peak occurs directly above an interval of very light sediments (Fig. 10b) with maximum carbonate (and very low K -) content characterizing MIS 11. Furthermore the age control is confirmed by similarity of the U1475 L* with the global benthic isotope stack (Fig. 10b).

MIS 11 is globally marked by increased $CaCO_3$ accumulation but also by enhanced carbonate dissolution (Barker et al., 2006). At Site U1475, MIS 11 correlates with a minimum in P-wave velocity at 11.5 m CCSF-B (Fig. 5a) that could be due to a dissolution-induced dominance of finer grain sizes in the carbonate fraction. But the velocity minimum does not cause reflector Purple since density at the same depth exhibits a maximum (Fig. 5b) leading to relatively constant impedance (Fig. 5c) in this interval. Instead, reflector Purple is caused by impedance decrease towards the glacial inception of MIS 10 (Fig. 10b).

We postulate that the density/impedance drop at MIS10 is attributed to enhanced terrigenous supply during a time of rapid decrease in NADW influence over the AP and replacement by southern sourced waters as inferred for the younger glacial intervals (Molyneux et al., 2007). Upward from reflector Purple seismic impedance mirrors glacial /interglacial cycles with higher impedance and carbonate content (lower wt% K, higher L*) characterizing interglacial MIS (Fig. 10b).

6 Conclusions

We present a new seismic stratigraphy for the late Miocene to Pleistocene at the AP that is based on carefully edited and in situ corrected high-resolution physical property core logging data of IODP Site U1475. A synthetic seismogram allows accurate traveltime-depth conversions and ties to an age model that is based on bio- and magnetostratigraphic datums. The six identified marker horizons are here described for the first time and occur above previously dated horizons.

Two reflectors dated at the late Miocene (~5.7±0.5 Ma) and the early Pliocene (~4.1±0.4 Ma) bound a peculiar high sedimentation rate interval that is characterized by the development of sediment waves and likely represents a time of strong AMOC with maximized flow of NADW in Indian-Atlantic Ocean gateway.

A reflector of moderate strength and an assigned age of ~2.7±0.3 Ma correlates with the intensification of Northern Hemisphere Glaciation (iNHG) and possibly represents one of the larger glacial inceptions (MIS G10 or G6) following the final closure of the Central American Seaway (CAS).

At the early Pleistocene transition (~1.5±0.3 Ma) another strong reflector, related to enhanced carbonate sedimentation, marks a glacial termination, which likely precedes the prominent “warm” MIS 47 and 49.

Two high amplitude reflectors occur within the late Pleistocene sequence at the transitions from interglacial to glacial stages at ~ 0.36 ± 0.02 Ma and 0.80 ± 0.05 Ma. Both reflectors are associated with cooling following the prominent interglacial MIS 11 and the beginning of the mid Pleistocene transition (MPT), respectively.

In summary, we have shown that the most prominent global climate and oceanographic changes of the last 7 Ma left a marked imprint in the physical structure of a sediment drift at the AP. The detailed stratigraphic and geochemical analyses necessary to establish a more precise timing of the reflection events are beyond the scope of this study, but will be the subject of future work. Thus, the presented correlations are general, but they strongly emphasize that Site U1475 provides an ideal archive for high-resolution paleo-oceanographic reconstructions. In this context, the high sedimentation rates of ~10 cm/kyr in the interval ~3.9 - 5.3 Ma make the site especially suitable to achieve millennial-scale paleoceanographic objectives for the Pliocene.

Appendix A

A1. Author Contributions

J.G. coordinated the writing effort and drafted most figures; F.J.E., N.L. and J.G. measured physical properties during IODP Exp. 361; G.U. provided and interpreted the seismic data; F.J.E., N.L. and G.U. contributed to the discussions; I.H., S.H. and L.L. led Expedition 361 and edited drafts. All coauthors were participants on IODP Expedition 361 and participated in generating the ship-board data.

A2. Additional IODP Expedition 361 Scientists

S. Barker[1], M.A. Berke[2], L. Brentegani[3], T. Caley[4], A. Cartagena-Sierra[2], C.D. Charles[5], J.J. Coenen[6], J.G. Crespin[4], A.M. Franzese[7], X. Han[8], S.K.V. Hines[9], J. Just[10], A. Koutsodendris[11], K. Kubota[12], R.D. Norris[5], T.P. Santos[13], R. Robinson[14], J.M. Rolinson[15], M.H. Simon[16], D. Tangunan[17], H.J.L. van der Lubbe[18], M. Yamane[19], and H. Zhang[20].

[1]School of Earth and Ocean Sciences, Cardiff University, Cardiff, UK, [2]Department of Civil and Environmental Engineering and Earth Sciences, University of Notre Dame, Notre Dame, USA, [3]Earth and Environmental Sciences, University of Technology Queensland, Brisbane, Australia, [4]EPOC, UMR CNRS 5805, University of Bordeaux, Pessac, France, [5]Scripps Institution of Oceanography, University of California, San Diego, La Jolla, USA,

[6]Department of Geology, Northern Illinois University, DeKalb, IL 60115, USA, [7]Natural Sciences Department, School of Earth and Environmental Sciences, Hostos Community College (C.U.N.Y.), Bronx NY, USA, [8]Second Institute of Oceanography (SOA), Key Laboratory of Submarine Science, Hangzhou City, P.R. China, [9]Division of Geological and Planetary Sciences, California Institute of Technology, Pasadena, USA, [10]Geologisches Institut, Universität Köln, Germany [11]Institute of Earth Sciences, Heidelberg University, Heidelberg, Germany, [12]Atmosphere and Ocean Research Institute, University of Tokyo, Kashiwashi Chiba, Japan, [13]Programa de Geociências (Geoquímica), Universidade Federal Fluminense, Niterói, Brazil, [14]Graduate School of Oceanography, University of Rhode Island, Narragansett, USA, [15]Chemistry Department, University of Otago, Dunedin, New Zealand, [16]NORCE Norwegian Research Centre, Bjerknes Centre for Climate Research, Bergen, Norway, [17]Department of Geosciences, University of Bremen, Bremen, Germany, [18]Department of Earth Sciences, Cluster Geochemistry & Geology, Vrije Universiteit VU, Amsterdam, the Netherlands, [19]Department of Biogeochemistry, Japan Agency for Marine-Earth Science and Technology (JAMSTEC), Yokosuka, Japan, [20]Lab of Plateau Lake Ecology and Global Change, Yunnan Normal University, Kunming Chengong, P.R. China

Acknowledgments

We acknowledge the work of the crew, technicians, and scientific staff of IODP Expedition 361. This research used samples and data provided by the International Ocean Discovery Program (IODP). Funding was provided by the Deutsche Forschungsgemeinschaft (DFG) under contract UE 49/17. Comments by Andrew Green and an anonymous reviewer greatly improved our manuscript. The data reported here are available through the Pangaea database (https://doi.org/10.1594/PANGAEA.896810).

References

Allen, R. B., & Tucholke, B. E. (1981). Petrography and implications of continental rocks from the Agulhas Plateau, southwest Indian Ocean. *Geology, 9*(10), 463-468. https://doi.org/10.1130/0091-7613(1981)9%3C463:PAIOCR%3E2.0.CO;2

Arhan, M., Mercier, H., & Park, Y.-H. (2003). On the deep water circulation of the eastern South Atlantic Ocean. *Deep-Sea Research Part I-Oceanographic Research Papers, 50*(7), 889-916. https://doi.org/10.1016/S0967-0637(03)00072-4

Arhan, M., Speich, S., Messager, C., Dencausse, G., Fine, R., & Boye, M. (2011). Anticyclonic and cyclonic eddies of subtropical origin in the subantarctic zone south of Africa. *Journal of Geophysical Research-Oceans, 116*. https://doi.org/10.1029/2011JC007140

Barker, S., Archer, D., Booth, L., Elderfield, H., Henderiks, J., & Rickaby, R. E. M. (2006). Globally increased pelagic carbonate production during the Mid-Brunhes dissolution interval and the CO2 paradox of MIS 11. *Quaternary Science Reviews, 25*(23-24), 3278-3293. https://doi.org/10.1016/j.quascirev.2006.07.018

Beal, L. M., De Ruijter, W. P. M., Biastoch, A., & Zahn, R. (2011). On the role of the Agulhas system in ocean circulation and climate. *Nature, 472*(7344), 429-436. https://doi.org/10.1038/nature09983

Bell, D. B., Jung, S. J. A., Kroon, D., Lourens, L. J., & Hodell, D. A. (2014). Local and regional trends in Plio-Pleistocene δ18O records from benthic foraminifera. *Geochemistry, Geophysics, Geosystems, 15*(8), 3304-3321. https://doi.org/10.1002/2014GC005297

Best, A. I., & Gunn, D. E. (1999). Calibration of marine sediment core loggers for quantitative acoustic impedance studies. *Marine Geology, 160*(1-2), 137-146. https://doi.org/10.1016/S0025-3227(99)00017-1

Billups, K. (2002). Late Miocene through early Pliocene deep water circulation and climate change viewed from the sub-Antarctic South Atlantic. *Palaeogeography, Palaeoclimatology, Palaeoecology, 185*(3-4), 287-307. https://doi.org/10.1016/S0031-0182(02)00340-1

Boyer, T. P., Antonov, J. I., Baranova, O. K., Coleman, C., Garcia, H. E., Grodsky, A., et al. (2013). World Ocean Database 2013 *NOAA Atlas NESDIS 72* (pp. 288). Silver Spring, MD: NOAA Printing Office. https://doi.org/10.7289/V5NZ85MT

Brierley, C. M., Fedorov, A. V., Liu, Z., Herbert, T. D., Lawrence, K. T., & LaRiviere, J. P. (2009). Greatly Expanded Tropical Warm Pool and Weakened Hadley Circulation in the Early Pliocene. *Science, 323*(5922), 1714. https://doi.org/10.1126/science.1167625

Castelino, J. A., Reichert, C., & Jokat, W. (2017). Response of Cenozoic turbidite system to tectonic activity and sea-level change off the Zambezi Delta. *Marine Geophysical Research, 38*(3), 209-226. https://doi.org/10.1007/s11001-017-9305-8

Christensen, B. A., Renema, W., Henderiks, J., De Vleeschouwer, D., Groeneveld, J., Castañeda, I. S., et al. (2017). Indonesian Throughflow drove Australian climate from humid Pliocene to arid Pleistocene. *Geophysical Research Letters, 44*(13), 6914-6925. https://doi.org/10.1002/2017GL072977

Cronin, M. F., Tozuka, T., Biastoch, A., Durgadoo, J. V., & Beal, L. M. (2013). Prevalence of strong bottom currents in the greater Agulhas system. *Geophysical Research Letters, 40*(9), 1772-1776. https://doi.org/10.1002/grl.50400

Davidson, J. M., Biggar, J. W., & Nielsen, D. R. (1963). Gamma-radiation attenuation for measuring bulk density and transient water flow in porous materials. *Journal of Geophysical Research, 68*(16), 4777-4783. https://doi.org/10.1029/JZ068i016p04777

De Vleeschouwer, D., Dunlea, A. G., Auer, G., Anderson, C. H., Brumsack, H., de Loach, A., et al. (2017). Quantifying K, U, and Th contents of marine sediments using shipboard natural gamma radiation spectra measured on DVJOIDESResolution. *Geochemistry, Geophysics, Geosystems, 18*(3), 1053-1064. https://doi.org/10.1002/2016GC006715

Evans, H. B. (1965). *GRAPE* - A Device For Continuous Determination Of Material Density And Porosity*. Paper presented at the SPWLA 6th Annual Logging Symposium (Volume II), 4-7 May, Dallas, Texas.

Fischer, M. D., & Uenzelmann-Neben, G. (2018). Late Cretaceous onset of current controlled sedimentation in the African–Southern Ocean gateway. *Marine Geology*, *395*, 380-396. https://doi.org/10.1016/j.margeo.2017.11.017

Flood, R. D. (1988). A lee wave model for deep-sea mudwave activity. *Deep Sea Research Part A. Oceanographic Research Papers, 35*(6), 973-983. https://doi.org/10.1016/0198-0149(88)90071-4

Gerland, S., & Villinger, H. (1995). Nondestructive density determination on marine sediment cores from gamma-ray attenuation measurements. *Geo-Marine Letters*, *15*(2), 111-118. https://doi.org/10.1007/BF01275415

Gohl, K., Uenzelmann-Neben, G., & Grobys, N. (2012). Growth and dispersal of a Southeast African large Igneous Province. *South African Journal of Geology*, *114*(3-4), 379. https://doi.org/10.2113/gssajg.114.3-4.379

Gruetzner, J., & Uenzelmann-Neben, G. (2016). Contourite drifts as indicators of Cenozoic bottom water intensity in the eastern Agulhas Ridge area, South Atlantic. *Marine Geology*, *378*, 350-360. https://doi.org/10.1016/j.margeo.2015.12.003

Gruetzner, J., Uenzelmann-Neben, G., Franke, D., & Arndt, J. E. (2014). Slowdown of Circumpolar Deepwater flow during the Late Neogene: Evidence from a mudwave field at the Argentine continental slope. *Geophysical Research Letters, 41*(6), 270-276. https://doi.org/10.1002/2014GL059581

Haarsma, R. J., Campos, E. J. D., Drijfhout, S., Hazeleger, W., & Severijns, C. (2011). Impacts of interruption of the Agulhas leakage on the tropical Atlantic in coupled ocean–atmosphere simulations. *Climate Dynamics*, *36*(5), 989-1003. https://doi.org/10.1007/s00382-009-0692-7

Hall, I. R., Hemming, S. R., LeVay, L. J., Barker, S., Berke, M. A., Brentegani, L., et al. (2017a). Expedition 361 methods. In I. R. Hall, Hemming, S.R., LeVay, L.J., and the Expedition 361 Scientists (Ed.), *South African Climates (Agulhas LGM Density Profile), Proceedings of the International Ocean Discovery Program*, *361*. College Station, TX: International Ocean Discovery Program. https://doi.org/10.14379/iodp.proc.361.102.2017

Hall, I. R., Hemming, S. R., LeVay, L. J., Barker, S., Berke, M. A., Brentegani, L., et al. (2017b). Expedition 361 summary. In I. R. Hall, Hemming, S.R., LeVay, L.J., and the Expedition 361 Scientists (Ed.), *South African Climates (Agulhas LGM Density Profile), Proceedings of the International Ocean Discovery Program*, *361*. College Station, TX: International Ocean Discovery Program. https://doi.org/10.14379/iodp.proc.361.101.2017

Hall, I. R., Hemming, S. R., LeVay, L. J., Barker, S., Berke, M. A., Brentegani, L., et al. (2017c). Site U1475. In I. R. Hall, Hemming, S.R., LeVay, L.J., and the Expedition 361 Scientists (Ed.), *South African Climates (Agulhas LGM Density Profile), Proceedings of the International Ocean Discovery Program*, *361*. College Station, TX: International Ocean Discovery Program. https://doi.org/10.14379/iodp.proc.361.104.2017

Hamilton, E. L. (1976). Variations of density and porosity with depth in deep-sea sediments. *Journal of Sedimentary Research*, *46*(2). https://doi.org/10.1306/212F6F3C-2B24-11D7-8648000102C1865D

Hays, J. D., Imbrie, J., & Shackleton, N. J. (1976). Variations in Earths Orbit - Pacemaker of Ice Ages. *Science*, *194*(4270), 1121-1132. https://doi.org/10.1126/science.194.4270.1121

Hernández-Guerra, A., & Talley, L. D. (2016). Meridional overturning transports at 30°S in the Indian and Pacific Oceans in 2002–2003 and 2009. *Progress in Oceanography*, *146*, 89-120. https://doi.org/10.1016/j.pocean.2016.06.005

Hodell, D. A., Curtis, J. H., Sierro, F. J., & Raymo, M. E. (2001). Correlation of late Miocene to early Pliocene sequences between the Mediterranean and North Atlantic. *Paleoceanography*, *16*(2), 164-178. https://doi.org/10.1029/1999PA000487

Hodell, D. A., & Venz-Curtis, K. A. (2006). Late Neogene history of deepwater ventilation in the Southern Ocean. *Geochem. Geophys. Geosyst.*, *7*(9), Q09001. https://doi.org/10.1029/2005GC001211

Ivanovic, R. F., Valdes, P. J., Flecker, R., & Gutjahr, M. (2014). Modelling global-scale climate impacts of the late Miocene Messinian Salinity Crisis. *Clim. Past, 10*(2), 607-622. https://doi.org/10.5194/cp-10-607-2014

Jaccard, S. L., Hayes, C. T., Martínez-García, A., Hodell, D. A., Anderson, R. F., Sigman, D. M., & Haug, G. H. (2013). Two Modes of Change in Southern Ocean Productivity Over the Past Million Years. *Science, 339*(6126), 1419-1423. https://doi.org/10.1126/science.1227545

Karas, C., Nürnberg, D., Bahr, A., Groeneveld, J., Herrle, J. O., Tiedemann, R., & deMenocal, P. B. (2017). Pliocene oceanic seaways and global climate. *Scientific Reports, 7*, 39842. https://doi.org/10.1038/srep39842

Karas, C., Nürnberg, D., Tiedemann, R., & Garbe‐Schönberg, D. (2011). Pliocene Indonesian Throughflow and Leeuwin Current dynamics: Implications for Indian Ocean polar heat flux. *Paleoceanography, 26*(2). https://doi.org/10.1029/2010PA001949

Lisiecki, L. E. (2014). Atlantic overturning responses to obliquity and precession over the last 3 Myr. *Paleoceanography, 29*(2), 71-86. https://doi.org/10.1002/2013PA002505

Lisiecki, L. E., & Herbert, T. D. (2007). Automated composite depth scale construction and estimates of sediment core extension. *Paleoceanography, 22*(4). https://doi.org/10.1029/2006PA001401

Lisiecki, L. E., & Raymo, M. E. (2005). A Pliocene-Pleistocene stack of 57 globally distributed benthic d18O records. *Paleoceanography, 20*(1), PA1003. https://doi.org/10.1029/2004PA001071

Lutjeharms, J. R. E. (1996). The Exchange of Water Between the South Indian and South Atlantic Oceans. In G. Wefer, W. Berger, G. Siedler, & D. J. Webb (Eds.), *The South Atlantic: Present and Past Circulation* (pp. 125-162). Berlin, Heidelberg: Springer Berlin Heidelberg. https://doi.org/10.1007/978-3-642-80353-6_8

Lutjeharms, J. R. E. (2007). Three decades of research on the greater Agulhas Current. *Ocean Sci., 3*(1), 129-147. https://doi.org/10.5194/os-3-129-2007

Lutjeharms, J. R. E., & Ansorge, I. J. (2001). The Agulhas Return Current. *Journal of Marine Systems, 30*(1), 115-138. https://doi.org/10.1016/S0924-7963(01)00041-0

Macdonald, A. M. (1993). Property fluxes at 30°S and their implications for the Pacific-Indian throughflow and the global heat budget. *Journal of Geophysical Research: Oceans, 98*(C4), 6851-6868. https://doi.org/10.1029/92JC02964

Mackenzie, K. V. (1981). Nine-term equation for sound speed in the oceans. *The Journal of the Acoustical Society of America, 70*(3), 807-812. https://doi.org/10.1121/1.386920

Marino, G., Zahn, R., Ziegler, M., Purcell, C., Knorr, G., Hall, I. R., et al. (2013). Agulhas salt-leakage oscillations during abrupt climate changes of the Late Pleistocene. *Paleoceanography, 28*(3), 599-606. https://doi.org/10.1002/palo.20038

Mayer, L. A. (1980). Deep-Sea Carbonates - Physical Property Relationships and the Origin of High-Frequency Acoustic Reflectors. *Marine Geology, 38*(1-3), 165-183. https://doi.org/10.1016/0025-3227(80)90057-2

Mayer, L. A. (1991). Extraction of high-resolution carbonate data for palaeoclimate reconstruction. *Nature, 352*, 148. https://doi.org/10.1038/352148a0

Mayer, L. A., Shipley, T. H., Theyer, F., Wilkens, R. H., & Winterer, E. L. (1985). Seismic modeling and paleoceanography at Deep Sea Drilling Project Site 574. In L. A. Mayer, F. Theyer, J. A. Barron, D. A. Dunn, T. Handyside, S. Hills, I. Jarvis, C. A. Nigrini, N. G. Pisias, A. Pujos, T. Saito, P. M. Stout, E. Thomas, N. Weinreich, R. H. Wilkens, & M. G. Bailey (Eds.), *Initial Reports of the Deep Sea Drilling Project* (Vol. 85, pp. 947-970): (U.S. Government Printing Office). https://doi.org/10.2973/dsdp.proc.85.132.1985

Mayer, L. A., Shipley, T. H., & Winterer, E. L. (1986). Equatorial Pacific Seismic Reflectors as Indicators of Global Oceanographic Events. *Science, 233*(4765), 761. https://doi.org/10.1126/science.233.4765.761

McCave, I. N. (2017). Formation of sediment waves by turbidity currents and geostrophic flows: A discussion. *Marine Geology, 390*, 89-93. https://doi.org/10.1016/j.margeo.2017.05.003

Miller, K. G., Kominz, M. A., Browning, J. V., Wright, J. D., Mountain, G. S., Katz, M. E., et al. (2005). The Phanerozoic Record of Global Sea-Level Change. *Science, 310*(5752), 1293-1298. https://doi.org/10.1126/science.1116412

Millero, F. J., Chen, C.-T., Bradshaw, A., & Schleicher, K. (1980). A new high pressure equation of state for seawater. *Deep Sea Research Part A. Oceanographic Research Papers, 27*(3), 255-264. https://doi.org/10.1016/0198-0149(80)90016-3

Molyneux, E. G., Hall, I. R., Zahn, R., & Diz, P. (2007). Deep water variability on the southern Agulhas Plateau: Interhemispheric links over the past 170 ka. *Paleoceanography, 22*(4), n/a-n/a. https://doi.org/10.1029/2006PA001407

Ohneiser, C., Florindo, F., Stocchi, P., Roberts, A. P., DeConto, R. M., & Pollard, D. (2015). Antarctic glacio-eustatic contributions to late Miocene Mediterranean desiccation and reflooding. *Nat Commun, 6*. https://doi.org/10.1038/ncomms9765

Parsiegla, N., Gohl, K., & Uenzelmann-Neben, G. (2008). The Agulhas Plateau: Structure and evolution of a Large Igneous Province. *Geophysical Journal International, 174*(1), 336-350. https://doi.org/10.1111/j.1365-246X.2008.03808.x

Pena, L. D., & Goldstein, S. L. (2014). Thermohaline circulation crisis and impacts during the mid-Pleistocene transition. *Science, 345*(6194), 318-322. https://doi.org/10.1126/science.1249770

Poore, H. R., Samworth, R., White, N. J., Jones, S. M., & McCave, I. N. (2006). Neogene overflow of Northern Component Water at the Greenland-Scotland Ridge. *Geochemistry Geophysics Geosystems, 7*. https://doi.org/10.1029/2005GC001085

Reghellin, D., Dickens, G. R., & Backman, J. (2013). The relationship between wet bulk density and carbonate content in sediments from the Eastern Equatorial Pacific. *Marine Geology, 344*(0), 41-52. https://doi.org/10.1016/j.margeo.2013.07.007

Ricker, N. (1953). The form and laws of propagation of seismic wavelets. *Geophysics, 18*(1), 10. https://doi.org/10.1190/1.1437843

Ritz, S. P., Stocker, T. F., Grimalt, J. O., Menviel, L., & Timmermann, A. (2013). Estimated strength of the Atlantic overturning circulation during the last deglaciation. *Nature Geosci, 6*(3), 208-212. https://doi.org/10.1038/ngeo1723

Rohling, E. J., Foster, G. L., Grant, K. M., Marino, G., Roberts, A. P., Tamisiea, M. E., & Williams, F. (2014). Sea-level and deep-sea-temperature variability over the past 5.3 million years. *Nature, 508*(7497), 477-482. https://doi.org/10.1038/nature13230

Romero, O. E., Kim, J. H., Bárcena, M. A., Hall, I. R., Zahn, R., & Schneider, R. (2015). High-latitude forcing of diatom productivity in the southern Agulhas Plateau during the past 350 kyr. *Paleoceanography, 30*(2), 2014PA002636. https://doi.org/10.1002/2014PA002636

Sarnthein, M. (2013). Transition from Late Neogene to Early Quaternary Environments. In S. A. Elias (Ed.), *The Encyclopedia of Quaternary Science* (Vol. 2, pp. 151-166). Amsterdam: Elsevier. https://doi.org/10.1016/B978-0-444-53643-3.00129-1

Schultheiss, P. J., & McPhail, S. D. (1989). An automated P-wave logger for recording fine-scale compressional wave velocity structures in sediments. In W. Ruddiman, M. Sarnthein, & e. al. (Eds.), *Proceedings of the Ocean Drilling Program, Scientific Results* (Vol. 108, pp. 407). Ocean Drilling Program, College Station, TX, United States: Texas A & M University. https://doi.org/10.2973/odp.proc.sr.108.157.1989

Steph, S., Tiedemann, R., Prange, M., Groeneveld, J., Nürnberg, D., Reuning, L., et al. (2006). Changes in Caribbean surface hydrography during the Pliocene shoaling of the Central American Seaway. *Paleoceanography, 21*(4), n/a-n/a. https://doi.org/10.1029/2004PA001092

Stichel, T., Frank, M., Rickli, J., & Haley, B. A. (2012). The hafnium and neodymium isotope composition of seawater in the Atlantic sector of the Southern Ocean. *Earth and Planetary Science Letters, 317–318*(0), 282-294. https://doi.org/10.1016/j.epsl.2011.11.025

Stow, D., Hunter, S., Wilkinson, D., & Hernández-Molina, F. (2008). The nature of contourite deposition. In M. Rebesco & A. Camerlenghi (Eds.), *Contourites* (Vol. 60, pp. 143-156).

Tucholke, B. E., & Carpenter, G. B. (1977). Sediment distribution and Cenozoic sedimentation patterns on the Agulhas Plateau. *Geological Society of America Bulletin, 88*(9), 1337-1346. https://doi.org/10.1130/0016-7606(1977)88%3C1337:SDACSP%3E2.0.CO;2

Tucholke, B. E., & Embley, R. W. (1984). Cenozoic regional erosion of the abyssal sea floor off South Africa. In J. S. Schlee (Ed.), *Interregional Unconformities and Hydrocarbon Accumulation* (Vol. 36, pp. 145-164): AAPG Memoir.

Uenzelmann-Neben, G. (2001). Seismic characteristics of sediment drifts: An example from the Agulhas Plateau, southwest Indian Ocean. *Marine Geophysical Researches, 22*(5), 323-343. https://doi.org/10.1023/A:1016391314547

Uenzelmann-Neben, G. (2002). Contourites on the Agulhas Plateau, SW Indian Ocean: indications for the evolution of currents since Palaeogene times. In D. Stow, J.-C. Faugeres, J. C. Howe, C. Pudsey, & A. Viana (Eds.), *Deep-water Contourite Systems : Modern Drifts and Ancient Series, Seismic and Sedimentary Characteristics* (Vol. 22, pp. 271-288). https://doi.org/10.1144/GSL.MEM.2002.022.01.20

Uenzelmann-Neben, G., Schlüter, P., & Weigelt, E. (2007). Cenozoic oceanic circulation within the South African gateway: indications from seismic stratigraphy. *South African Journal of Geology, 110*(2-3), 275-294. https://doi.org/10.2113/gssajg.110.2-3.275

Urmos, J., & Wilkens, R. H. (1993). In situ velocities in pelagic carbonates: New insights from Ocean Drilling Program Leg 130, Ontong Java Plateau. *Journal of Geophysical Research: Solid Earth, 98*(B5), 7903-7920. https://doi.org/10.1029/93JB00013

Urmos, J., Wilkens, R. H., Bassinot, F., Lyle, M., Marsters, J. C., Mayer, L. A., & Mosher, D. C. (1993). Laboratory and well-log velocity and density measurements from the Ontong Java Plateau; new in-situ corrections to laboratory data for pelagic carbonates. *Proceedings of the Ocean Drilling Program, Scientific Results, 130*, 607. https://doi.org/10.2973/odp.proc.sr.130.048.1993

Vasiliev, M. A., Blum, P., Chubarian, G., Olsen, R., Bennight, C., Cobine, T., et al. (2011). A new natural gamma radiation measurement system for marine sediment and rock analysis. *Journal of Applied Geophysics, 75*(3), 455-463. https://doi.org/10.1016/j.jappgeo.2011.08.008

Weijer, W., De Ruijter, W. P. M., Sterl, A., & Drujfhout, S. S. (2002). Response of the Atlantic overturning circulation to South Atlantic sources of buoyancy. *Global and Planetary Change, 34*(3-4), 293-311. https://doi.org/10.1016/S0921-8181(02)00121-2

Wiles, E., Green, A., Watkeys, M., Jokat, W., & Krocker, R. (2013). The evolution of the Tugela canyon and submarine fan: A complex interaction between margin erosion and bottom current sweeping, southwest Indian Ocean, South Africa. *Marine and Petroleum Geology, 44*, 60-70. https://doi.org/10.1016/j.marpetgeo.2013.03.012

Wiles, E., Green, A., Watkeys, M., Jokat, W., & Krocker, R. (2014). A new pathway for Deep water exchange between the Natal Valley and Mozambique Basin? *Geo-Marine Letters, 34*(6), 525-540. https://doi.org/10.1007/s00367-014-0383-1

Wyllie, M., Gregory, A., & Gardner, L. (1956). Elastic wave velocities in heterogeneous and porous media. *Geophysics, 21*(1), 41-70. https://doi.org/10.1190/1.1438217

Wynn, R. B., & Masson, D. G. (2008). Sediment Waves and Bedforms. In M. Rebesco & A. Camerlenghi (Eds.), *Contourites* (Vol. Volume 60, pp. 289-300): Elsevier. https://doi.org/10.1016/S0070-4571(08)10015-2

Wynn, R. B., & Stow, D. A. V. (2002). Classification and characterisation of deep-water sediment waves. *Marine Geology, 192*(1-3), 7-22. https://doi.org/10.1016/S0025-3227(02)00547-9

Ziegler, M., Diz, P., Hall, I. R., & Zahn, R. (2013). Millennial-scale changes in atmospheric CO2 levels linked to the Southern Ocean carbon isotope gradient and dust flux. *Nature Geosci, 6*(6), 457-461. https://doi.org/10.1038/ngeo1782

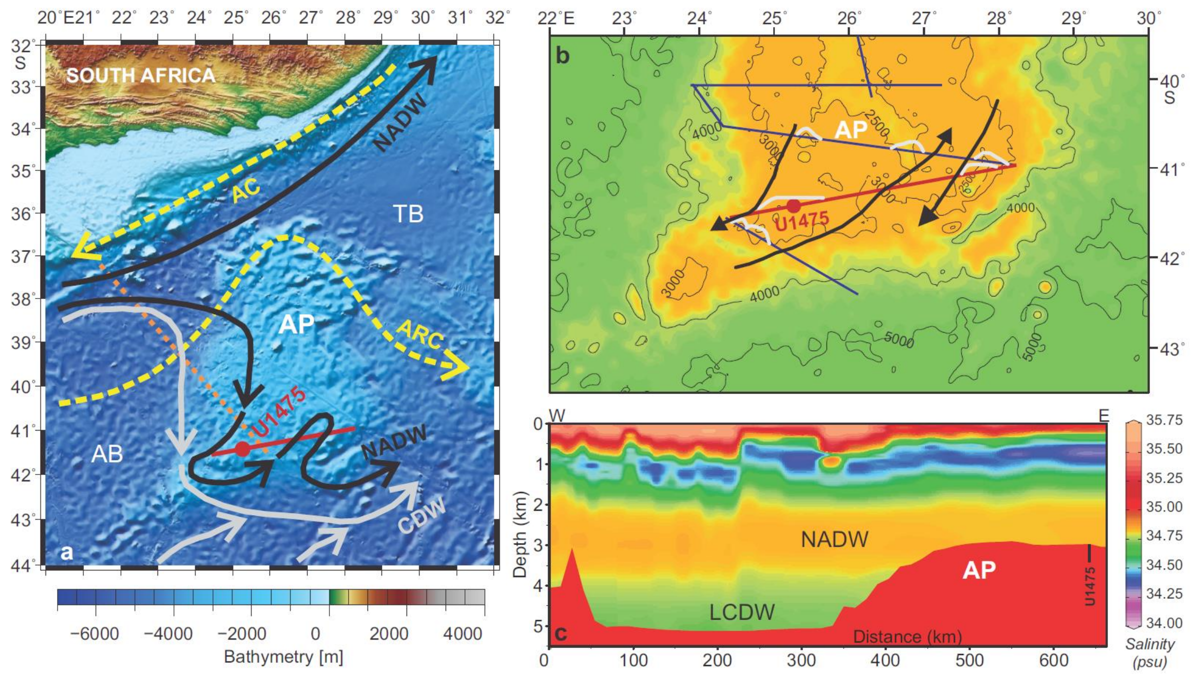

Figure 1. Geomorphologic and oceanographic features near IODP Site U1475 (a). Dashed yellow arrows = main surface currents (AC = Agulhas Current, ARC = Agulhas Return Current), solid arrows = bottom water currents (NADW = North Atlantic Deep Water, CDW = Circumpolar Deep Water), AP = Agulhas Plateau, AB= Agulhas Basin. Map (b) and cross section (c, dotted orange line in a) of present day salinity (color coded) over the southern Agulhas Plateau (Boyer et al., 2013) and IODP Site U1475 (projected). Contours in (b) refer to water depths in m. Arrows indicate bottom water circulation (Uenzelmann-Neben, 2002) inferred from the position and shape of sediment drifts (white mounded shapes) in seismic reflection profiles (straight lines). IODP Site U1475 and seismic profile AWI-98014 are marked in red in (a) and (b).

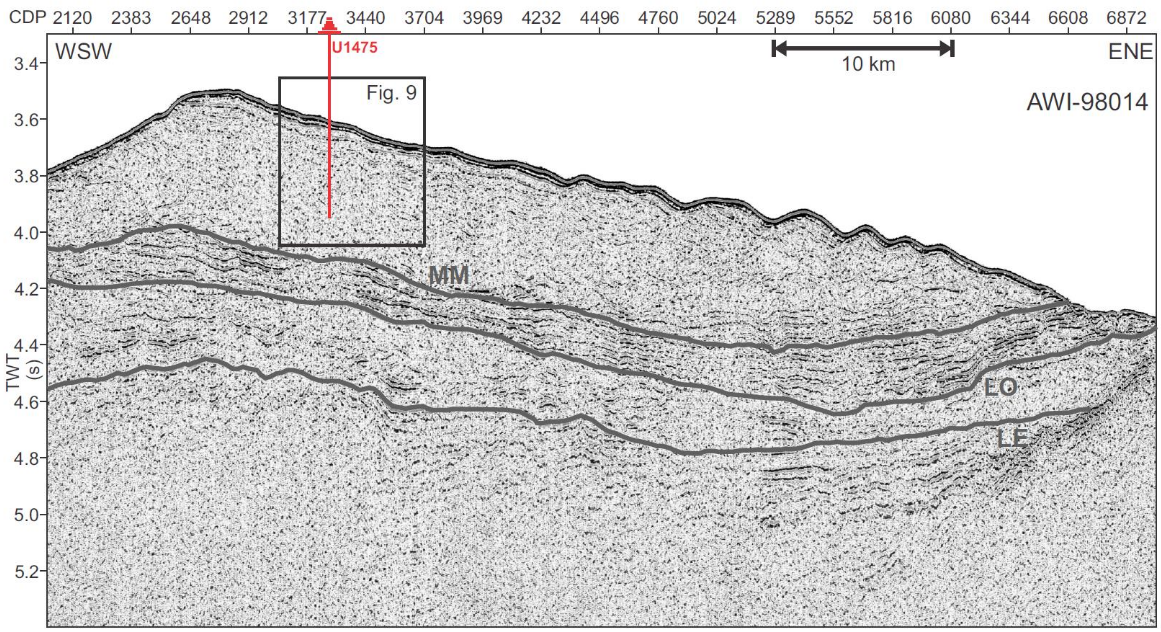

Figure 2. Western part of line AWI-98014 across IODP Site U1475 (red vertical line). The mounded asymmetric geometry of the sediment drift on the southwestern Agulhas Plateau is covered by wavy structures in the east. The base of the drift is formed by a band of strong reflections: LE = Lower Eocene, LO = Lower Oligocene, MM = Middle Miocene (Uenzelmann-Neben, 2001). Here, the drift appears seismically transparent. Its internal structure and the new seismic ties with the borehole are shown in Fig. 9.

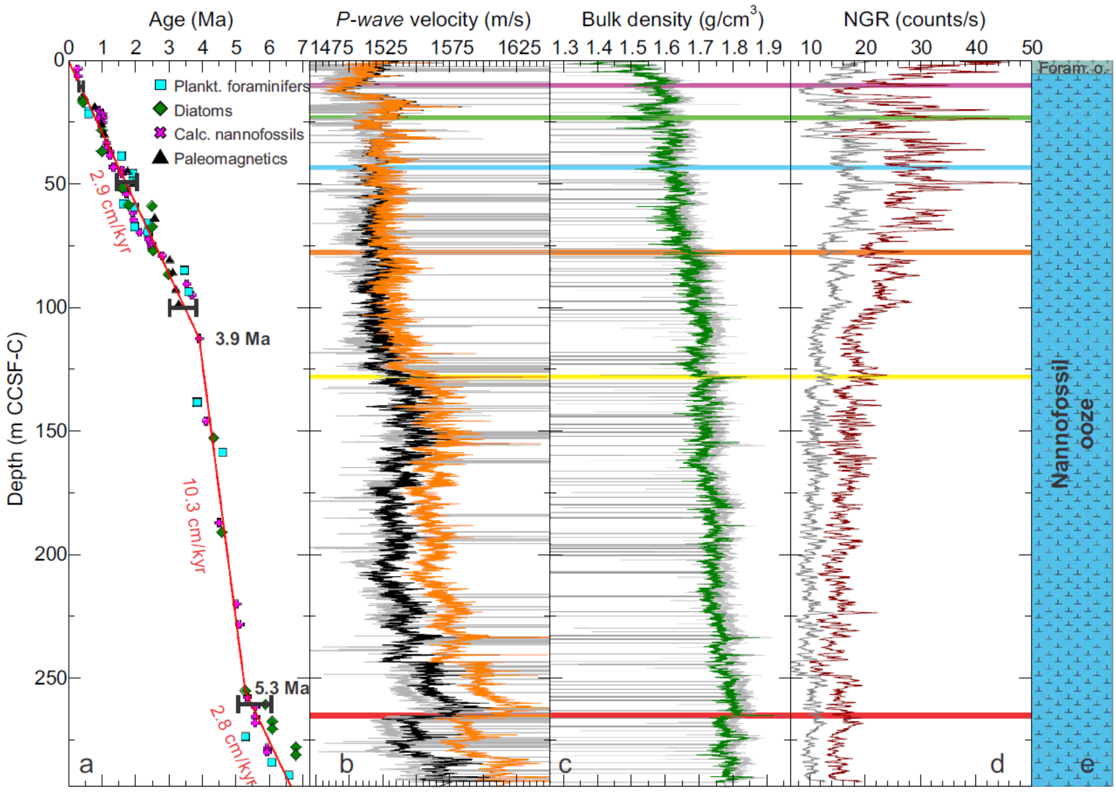

Figure 3. IODP Site U1475 data vs. depth (m CCSF-C): (a) Shipboard age model derived from bio- and magnetostratigraphy. Black bars indicate estimated age uncertainties. (b) Raw (grey), edited (black), and in situ corrected (orange) P-wave velocity. (c) Raw (grey) and edited (green) bulk density. (d) Raw (grey) and density corrected (dark red) natural gamma radiation (NGR). (e) Lithology (lithologic units I and II are shown in green and blue, respectively). Data resolution is 2.5 cm for velocity and density, and 10 cm for natural gamma radiation. Colored horizontal lines mark the positions of seismic reflectors.

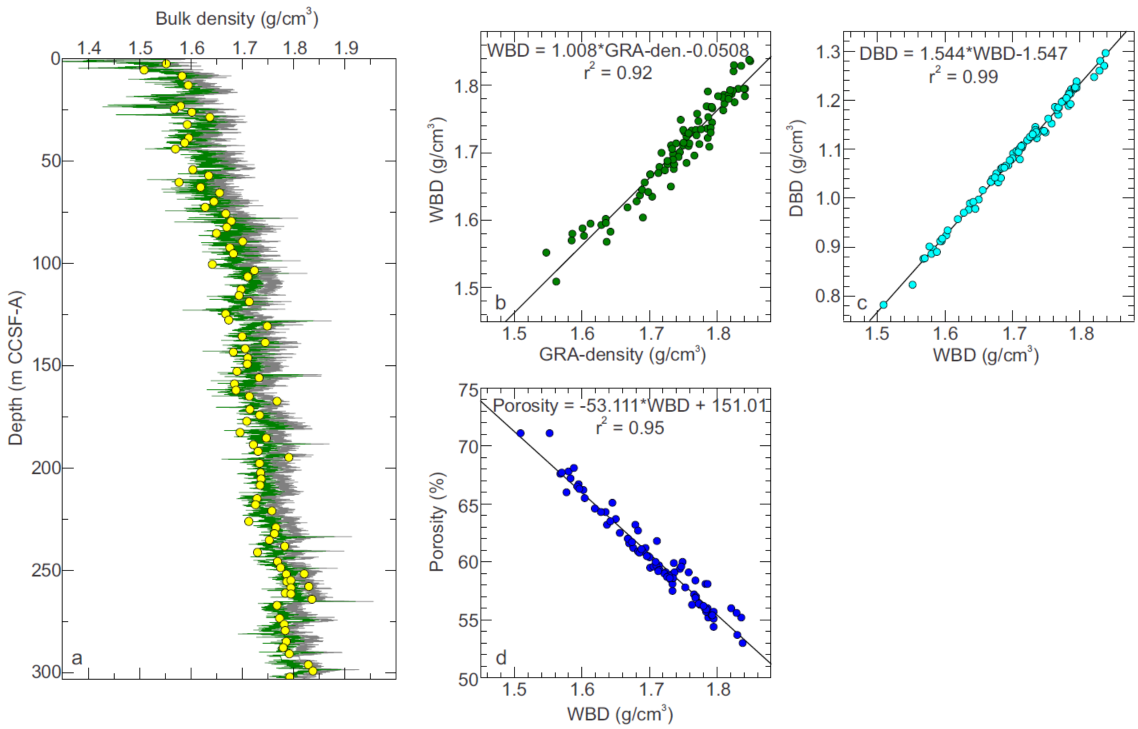

Figure 4. IODP Site U1475 density and porosity relationships: (a) Wet bulk density (WBD) measurements on discrete samples (yellow dots) in comparison to bulk density (green line) derived from edited shipboard GRA-density measurements (grey line) using the linear equation derived in (b), (b) GRA-bulk density vs. wet bulk density (WBD), (c) WBD vs. dry bulk density (DBD), (d) WBD vs. porosity.

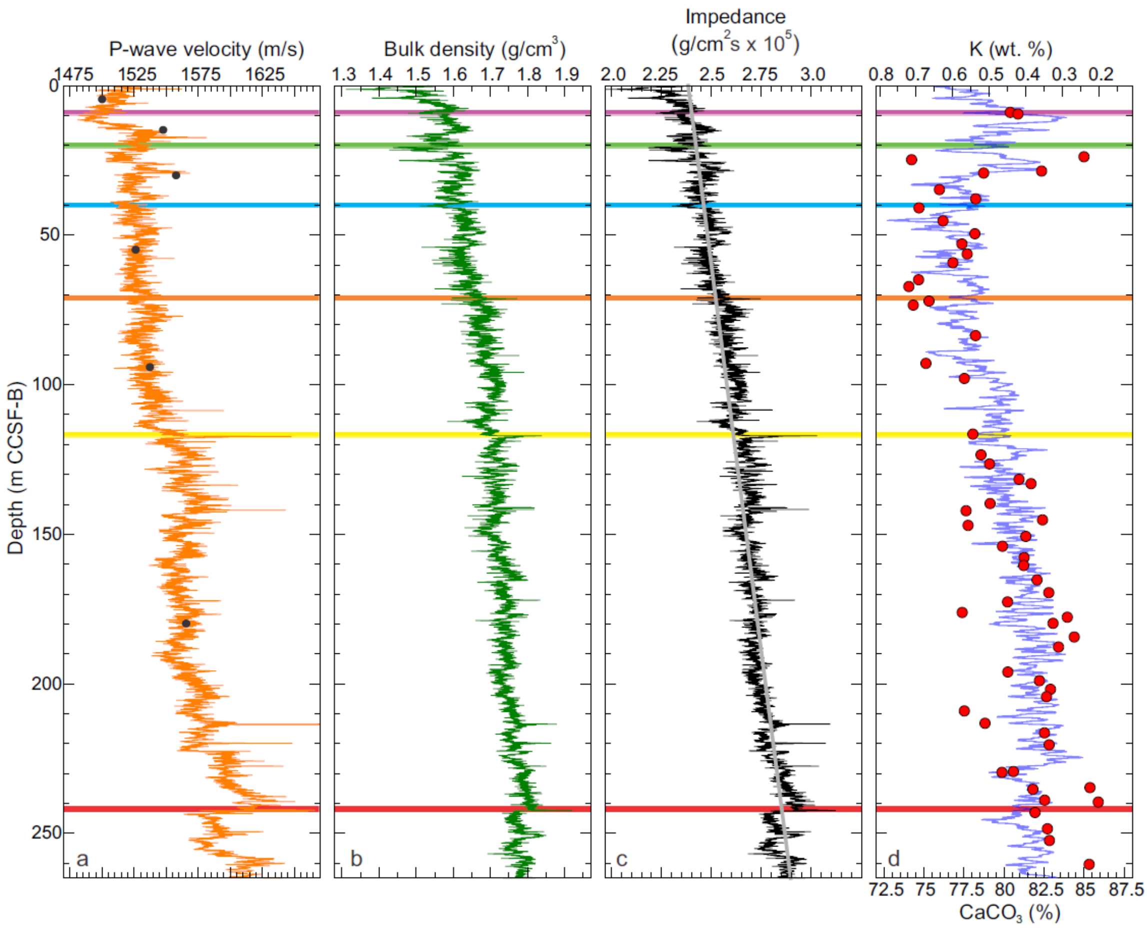

Figure 5. In situ corrected properties of (a) P-wave velocity, (b) bulk density, and (c) seismic impedance in comparison to (d) wt% Potassium (K, reverse scale) and discrete measurements of wt% $CaCO_3$ (red dots). Data are displayed on the CCSF-B depth scale, the in situ depth in meters below the seafloor (mbsf). Colored horizontal lines indicate the positions of seismic reflectors. Black dots in (a) mark interval velocities resulting from the synthetic time-depth ties. The compaction trend in impedance is indicated by a grey line.

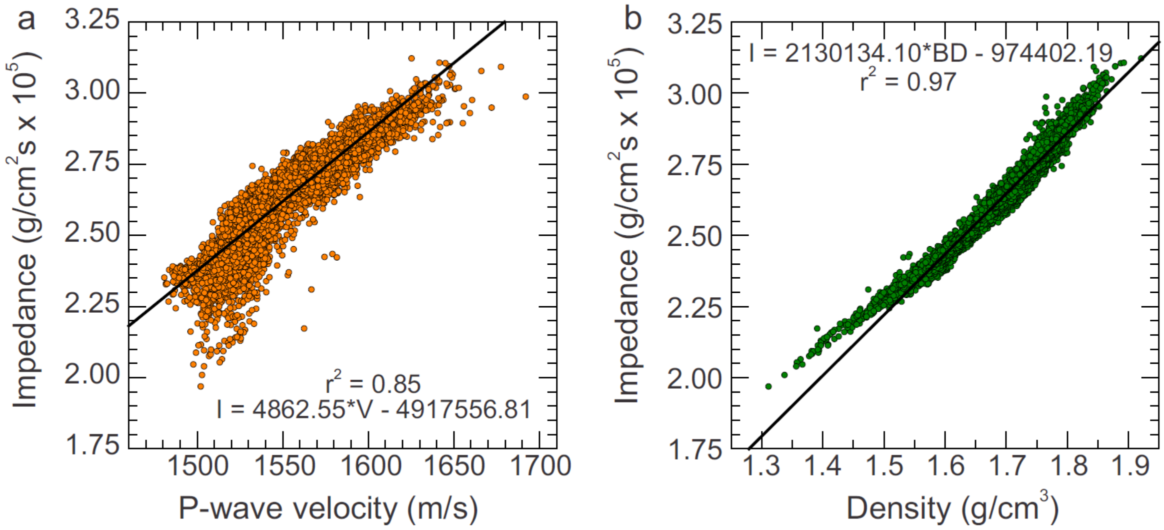

Figure 6. Linear regressions of seismic impedance vs. (a) *P-wave* velocity and (b) bulk density.

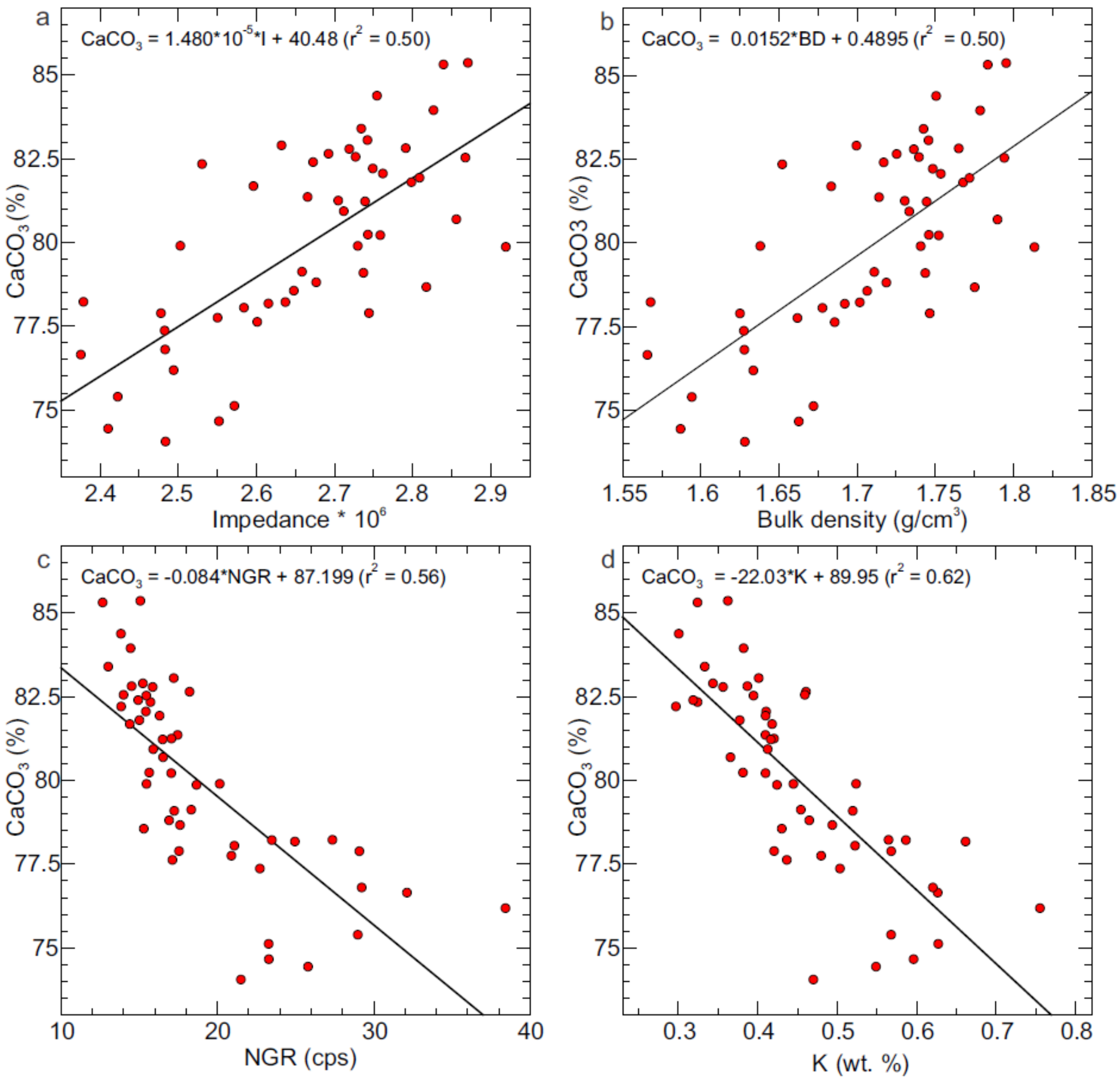

Figure 7. Linear regressions of carbonate content (wt% $CaCO_3$) vs. acoustic impedance (a), bulk density (b), natural gamma radiation (NGR) (b), and wt% potassium derived from NGR (d).

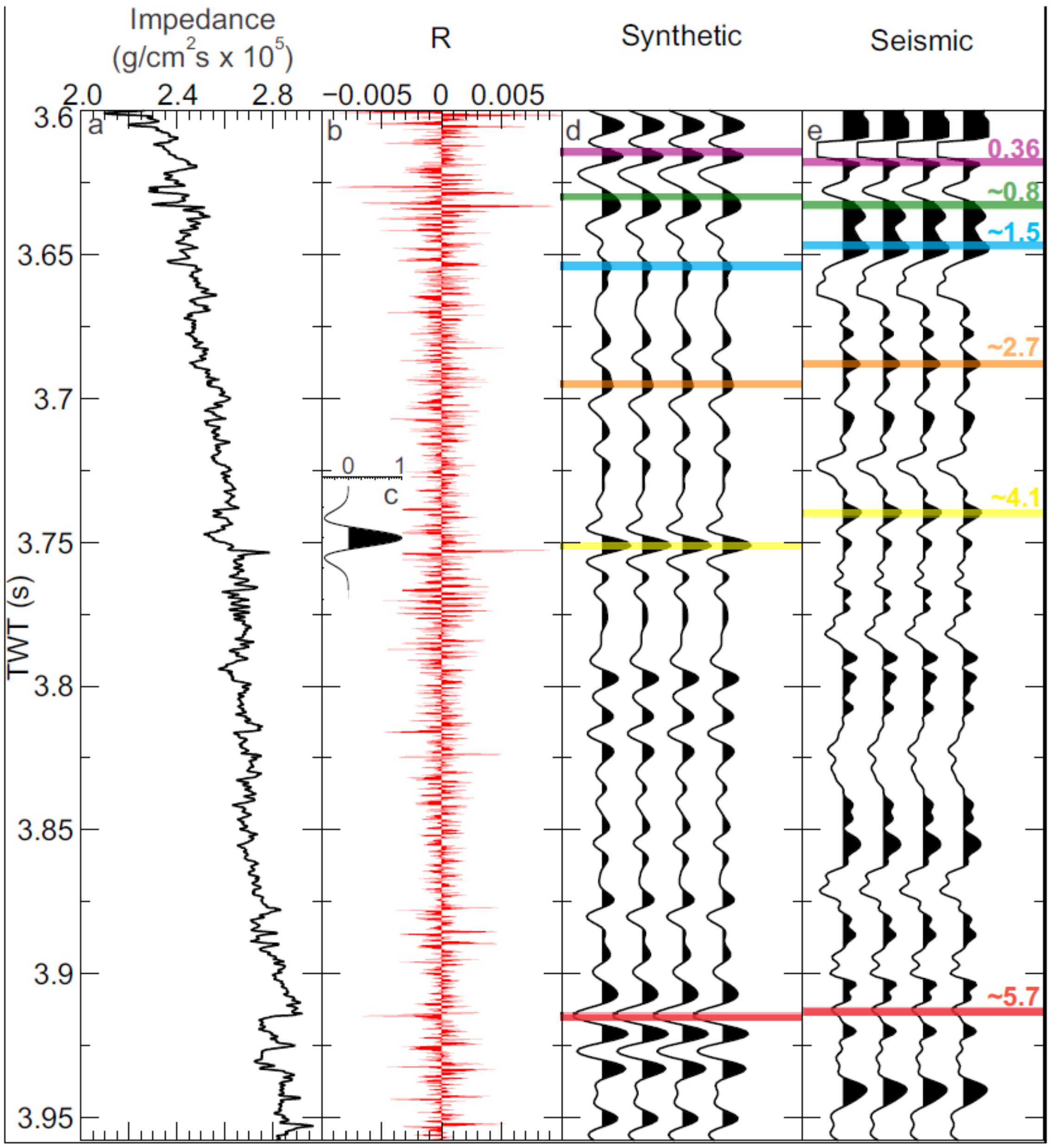

Figure 8. Seismic impedance (smoothed) (a), reflection coefficient (b), 65 Hz Ricker-wavelet (c) used to calculate the synthetic seismogram (d) at Site U1475 in comparison to seismic traces extracted from profile AWI-98014 in proximity to Site U1475 (e). Numbers in (e) are ages in Ma (see Table 1 for uncertainty estimations).

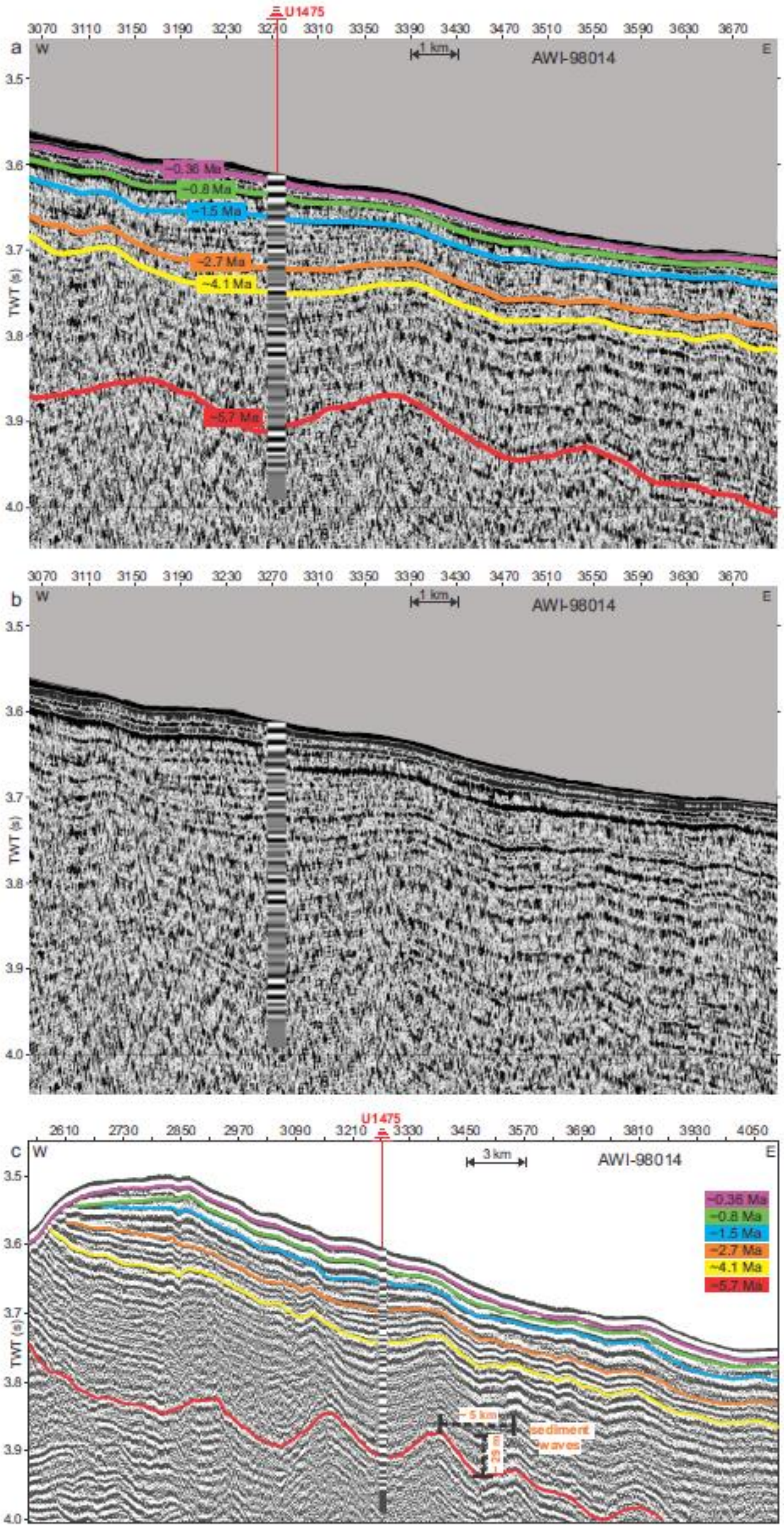
U1475
a
W
E
1 km
AWI-98014
~0.36 Ma
~0.8 Ma
~1.5 Ma
~2.7 Ma
~4.1 Ma
~5.7 Ma
TWT (s)
b
c
3 km
~5 km
sediment waves

Figure 9. (a) Interpreted section of multichannel seismic reflection profile AWI-98014 (Uenzelmann-Neben, 2001) across IODP Site U1475 (red vertical line), the synthetic seismogram calculated from Site U1475 data is overlain, interpreted reflectors are listed in Table 1, (b) uninterpreted section, (c) black and white plot (wider section, narrower band pass filter of 40-45 to 210-230 Hz) of the interpreted profile. The synthetic seismogram is overlain and stippled lines indicate dimensions of a selected sediment wave. Note that wave height degrades from ~ 29 m at reflector Red towards the seafloor.

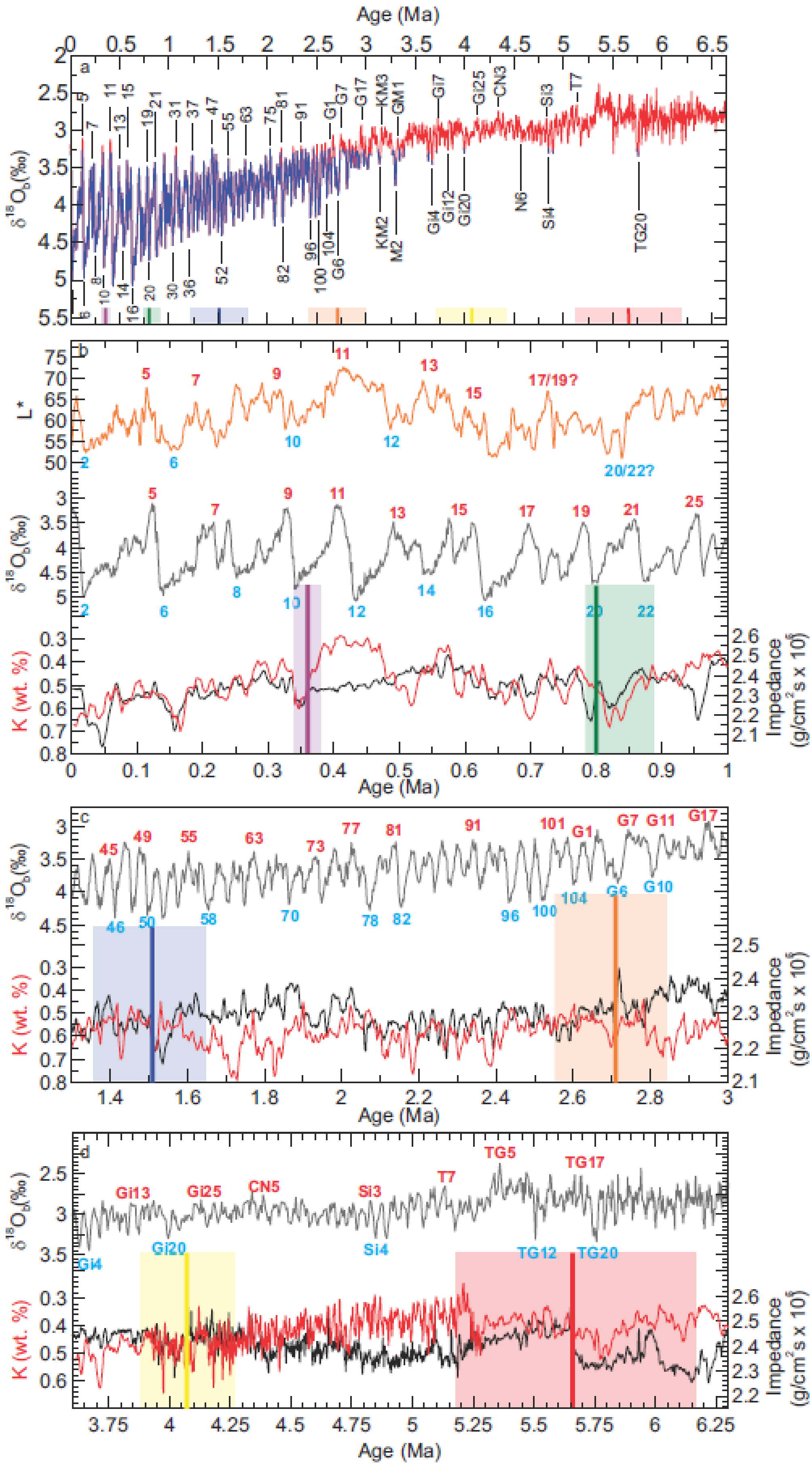
Age (Ma)
a
δ18Ob(‰)
b
L*
17/19?
20/22?
δ18Ob(‰)
K (wt. %)
Impedance (g/cm2s x 10^5)
Age (Ma)
c
δ18Ob(‰)
K (wt. %)
Impedance (g/cm2s x 10^5)
Age (Ma)
d
δ18Ob(‰)
K (wt. %)
Impedance (g/cm2s x 10^5)
Age (Ma)

Figure 10. (a) Age assignments of interpreted seismic reflectors (colored vertical lines, estimated age uncertainty is indicated by shaded backgrounds) on the Agulhas Plateau in comparison to a benthic oxygen isotope compilation of global ice volume changes over the last 6.6 Ma (δ^{18}O blue line < 3.25‰, modern value < δ^{18}O red line). The isotope compilation consists of the benthic δ^{18}O “LR04” (Lisiecki & Raymo, 2005) stack from 0-5.3 Ma extended to 6.6 Ma by the benthic δ^{18}O record of Site 982 (Hodell et al., 2001). Selected marine isotope stages (MIS) are indicated. (b-d) Selected enlarged intervals of (a) illustrating the position of the seismic reflectors in comparison to changes in global ice volume (benthic δ^{18}O, grey line with colored isotope stages), acoustic impedance (black line) and wt% potassium (K, red line, note reverse scale). Additionally, L* (lightness, orange line) from Site U1475 with identified MIS is plotted in (b) to show the accuracy of the used linear age model over the last 1 Ma. Reflector ages, impedance, wt% K and L* are shown on the age model derived from the Site U1475 bio- and magnetostratigraphic datums.

Table1

Traveltime to Major Reflectors as Picked from Field Record and Synthetic Seismogram, Site U1475

Reflector	Two way traveltime (s)		Depth (m CCSF-C)	Depth (m CCSF-B)	Age (Ma)
	Field record	Synthetic			
Purple	3.618	3.615	10.27	9.38	0.36±0.01
Green	3.635	3.630	22.96	20.98	0.80+0.07
Blue	3.648	3.654	43.43	39.68	1.51±0.30
Orange	3.688	3.695	77.66	70.96	2.71±0.30
Yellow	3.740	3.755	128.15	117.08	4.07±0.40
Red	3.913	3.915	265.29	242.39	5.66±0.50